Journal of Intelligent & Robotic Systems (2024) 110:66
https://doi.org/10.1007/s10846-024-02090-7

REGULAR PAPER

A Compact Aerial Manipulator: Design and Control for Dexterous Operations

Qianyuan Liu[1] · Yuhang Liu[2] · Zeshuai Chen[1] · Kexin Guo[2,3] · Xiang Yu[1,3] · Youmin Zhang[4] · Lei Guo[1,3]

Received: 19 September 2023 / Accepted: 11 March 2024 / Published online: 26 April 2024

Abstract
The lack of aerial physical interaction capability is one of the choke points limiting the extension of aerial robot applications, such as rescue missions and aerial maintenance. We present a new aerial robotic manipulator (AEROM) for aerial dexterous operations in this work. It contains a robotic manipulator with 6-degree-of-freedom and a compact flight platform. Firstly, we propose a quantitative capability index to evaluate and guide the mechanical design of the AEROM. Based on the proposed quantitative index, we construct a lightweight bird-inspired manipulator to imitate a raptor hindlimb. An additional telescopic joint and an end-effector consisting of three soft fingers allow the AEROM to execute aerial interaction tasks. In addition, the wrist joints enable independent control of the end-effector attitude regardless of the flight platform. After explicitly analyzing the multi-source disturbances during the aerial operation tasks, we develop a refined anti-disturbance controller to compensate for the disturbances with different characteristics. The proposed controller further improves the position accuracy of end-effector to enable dexterous operations during aerial interaction tasks. Finally, the physical experiments verify the effectiveness of the proposed AEROM system.

Keywords Aerial systems: Mechanics and control · Mobile manipulation · Aerial manipulation · Underactuated robots

1 Introduction

In recent years, aerial robotic manipulators (AEROMs) have received extensive attention [1] for the potential applications of accident response [2], removing foreign objects [3], special facility maintenance [4], and harsh environment surveys [5]. A classical AEROM consists of a flight platform and various robotic manipulators to physically interact with the environment. Flight platforms typically possess vertical take-off and landing capabilities to overcome terrain constraints. Unlike conventional multirotors, the AEROM is equipped with a customized manipulator to maneuver a target in the air. Therefore, the ability of AEROM to quickly reach and operate in a three-dimensional (3D) workspace is conducive to reducing time, cost, and risk for humans (e.g., building cleaning [6]).

✉ Kexin Guo
kxguo@buaa.edu.cn

✉ Xiang Yu
xiangyu_buaa@buaa.edu.cn

Extended author information available on the last page of the article

However, achieving an efficient AEROM requires more effort than simply attaching a robotic manipulator to a conventional unmanned aerial vehicle (UAV). The main challenges of integrating a UAV with a manipulator can be summarized as: (i) The compactness of AEROMs is crucial for enabling dexterous aerial operations. Thus, the center of mass (CoM) shift caused by the mounted manipulator cannot be neglected; (ii) The manipulator needs to ensure that the end-effector has adequate dexterity to track the desired spatial position and attitude simultaneously. Moreover, a versatile end-effector is indispensable for facilitating aerial physical interactions, encompassing actions such as pushing, screwing, and picking up objects; (iii) During dexterous aerial operations, it is essential to attenuate the impact of multi-source disturbances on flight performance. These disturbances include reaction forces on the end-effector, near-wall effects resulting from turbulence reflected from the surroundings, and mismatches in the AEROM dynamics.

Some existing studies have been carried out to address these challenges. With the evolution of AEROM design, researchers have utilized a wide range of aerial vehicles to provide maneuverability. These flight platforms are divided

into two categories depending on the rank of the control allocation matrix [7]. The flight platforms of the first category are under-actuated, where position and attitude are coupled, such as helicopter [8, 9], tricopter [10], quadcopter [11], and hexacopter [12, 13]. The second category of flight platforms has fully actuated property, whose position and attitude can be controlled independently, such as fully-actuated hexacopter [14] and omnidirectional hexacopter [15]. Although the fully-actuated flight platform offers the advantage of spot hovering at a specified attitude, its structural complexity hinders practical deployment compared to under-actuated platforms. Therefore, a four-axis multirotor structure is preferred due to its satisfactory compromise between flight efficiency and construction convenience.

The attached manipulator plays a crucial role in the AEROM system. Consequently, some studies have presented various manipulator prototypes with the diverse aerial interaction tasks that differ in the number of joints, joint structure, and arm types. For example, a two-finger gripper without joints is mounted on the belly of a conventional quadrotor to mimic raptor grasping [16]. Another conventional quadrotor is equipped with a sliding joint and a hook, which can install and retrieve sensors from a tree [2]. In [17], a 2 degree-of-freedom (DoF) lightweight manipulator is used to detect and map the welds on the industrial pipe. However, the restricted number of joints in these AEROM end-effectors hinders their ability to perform aerial dexterity operations. Therefore, the dexterous maneuvering of an end-effector necessitates additional joints to ensure adequate DoF.

With the level of maturity achieved, more articulated and functional aerial manipulators are emerging. In [18], a new AEROM is composed of a standard quadrotor and a 4-DoF manipulator, which is applied for visual-servo tasks. A large-load flight platform is equipped with a 7-DoF manipulator featuring redundant joints to enhance capture performance during bilateral teleoperation [19]. Furthermore, some studies have proposed different manipulator designs to compensate for external disturbances and achieve precise end-effector positioning, including parallel manipulators and multi-arm systems. For instance, a novel parallel 3-DoF manipulator is installed on an omnidirectional tilt-rotor to enhance end-effector tracking performance [20]. Additionally, there are ongoing studies on multiple arms, including manipulating long objects with dual arms [12], cooperative two-handed grasping [13], and landing on an uneven surface via three arms [21]. However, the utilization of parallel manipulators and multi-arm systems not only increases the mechanical complexity but also diminishes flight endurance.

During aerial dexterous operations, AEROMs face challenges in achieving stable and precise flight, limiting their full autonomy. Focusing on multirotor flight platforms, researchers have successfully applied several anti-disturbance control methods to mitigate the adverse effects of external disturbances (e.g., wind perturbation or hanging weight) [22–24]. Nevertheless, it is difficult to integrate a suitable controller for AEROMs. This is because high-precision end-effector positioning requires the flight platform to maintain satisfactory position tracking performance under unavoidable perturbations, particularly in the presence of multi-source disturbances. Hence, a variety of disturbance observer-based control (DOBC) methods have been investigated. In [25], an anti-disturbance attitude controller is proposed for an AEROM to improve trajectory tracking performance via DOBC. In [26], a robust controller is designed for an AEROM by formulating the dynamic coupling effects between the flight platform and the manipulator. Furthermore, as a classical anti-disturbance method, active disturbance rejection control (ADRC) has been utilized to effectively eliminate disturbances in the UAV attitude dynamics primarily caused by manipulator movements [27]. However, these free flight scenarios do not involve aerial physical interactions, which would otherwise require addressing more complex disturbances.

Therefore, an effective AEROM controller should counter the ticklish multi-source disturbances during aerial physical interactions. For the physical contacts, the paper [28] employs an optimization-based method by utilizing an onboard force/torque sensor to handle model uncertainties and external disturbances. The literature [29] presents a novel solution to tackle the issue of precise aerial physical interaction with the surroundings, including an enhanced momentum-based force estimator that avoids installing physical force sensors. Furthermore, the work [30] develops a nonlinear anti-disturbance controller to drive a movable structure (i.e., a rolling cart and hinged door), by considering the interaction force as a disturbance. However, these AEROMs performing physical interactions require sufficient joints and functional end-effectors for more aerial dexterous operations. Furthermore, the existing AEROM anti-disturbance methods [25, 30] exhibit some conservatism by considering multi-source disturbances as lumped disturbances. Therefore, incorporating prior knowledge of the multi-source disturbances can further enhance the AEROM performance by refining the characteristics of the disturbances.

Motivated by the challenges mentioned above, we focus on achieving dexterous aerial manipulations and precise physical interactions. In this work, we present an AEROM system comprising a compact flight platform and a multi-joint manipulator equipped with a versatile end-effector. In addition, several physical experiments demonstrate that the

designed AEROM has the ability to operate dexterously in the air. The major contributions of this work can be summarized as follows.

1. After comprehensively accommodating various vital characteristics that assess an AEROM, we propose a quantitative capability index. These characteristics include the controllable DoF of the end-effector, the maneuverability of flight platform, the workspace of mounted manipulator, the ability to operate the target, and the flight duration. Furthermore, we utilize this index to evaluate the AEROM performance and guide its construction in this study.
2. This paper presents a compact AEROM mechanism with a multirotor flight platform and a lightweight multi-joint manipulator. Compared with the existing aerial robotic systems for physical interactions [20, 28–31], the developed AEROM can independently control the position and attitude of the end-effector (consisting of three soft fingers), which is essential for dexterous manipulations. Further, unlike the classical AEROM, the developed flying platform is compact concerning the mounted manipulator dimensionality, which can operate the target dexterously, even when facing a vertical object surface.
3. Finally, we integrate a refined anti-disturbance controller (RADC) to stabilize the flight platform against multi-source disturbances (i.e., interaction force, external turbulence, the CoM shift, and the joint motion error) during aerial operations. In contrast to the DOBC or ADRC approaches [25–27, 30], the proposed controller uses partial prior knowledge to analyze the characteristics of multi-source disturbances. By this means, the multi-source disturbances can be estimated and compensated categorically to obtain higher performance instead of being treated as a lumped disturbance.

The remainder of the paper is structured as follows. Section 2 describes design of the AEROM architecture. Section 3 discusses the designed AEROM kinematic and dynamic model. Section 4 introduces the RADC for aerial dexterous operations. Section 5 showcases the system performance through a series of physical experiments. Lastly, Section 6 concludes the paper.

2 System Design

This section presents the design of the AEROM and the proposed structure. In our previous AEROM [32], we have identified two challenges that require reconstructing the hardware structure when the AEROM is in close proximity to the operation area. Firstly, as depicted in Fig. 1(a), the downwash airflow generated by the propeller can create a gust disturbance for the operating target, even causing the target to be blown away. Secondly, the near-wall effect may result in collisions due to the proximity to the corners, as illustrated in Fig. 1(b). Therefore, the conventional AEROM tends to be a large dimension without explicitly considering these two factors (e.g., 15-inch propeller [32]). Consequently, it may not fulfill the compactness requirements for aerial dexterous operations.

In fact, we have found that the manipulator workspace has an effect on the near-wall effect and gust disturbance in practical applications. Increasing the workspace relative to the flight platform leads to a reduction in the effect and disturbance. Consequently, we scale down the propellers to achieve a compact flight platform, as shown in Fig. 2. To increase the load capacity further, the flight platform is equipped with four propulsion units, which comprise coaxial rotors. Additionally, the counter-rotating propellers of equal size can mitigate the gyroscopic effect [15].

The compact flight platform presents a challenge for the mounted manipulator, as it needs to restrict weight utilization while ensuring the aerial dexterity of the end-effector. Inspired by the powerful hind limbs of an owl (see Fig. 3(a)), we design a lightweight robotic manipulator and attach it to the belly of the compact flight platform. As depicted in Fig. 3(b), the manipulator comprises multiple links forming a skeletal structure. Various revolute joints are positioned between the links, mimicking the tendons of an owl that drive

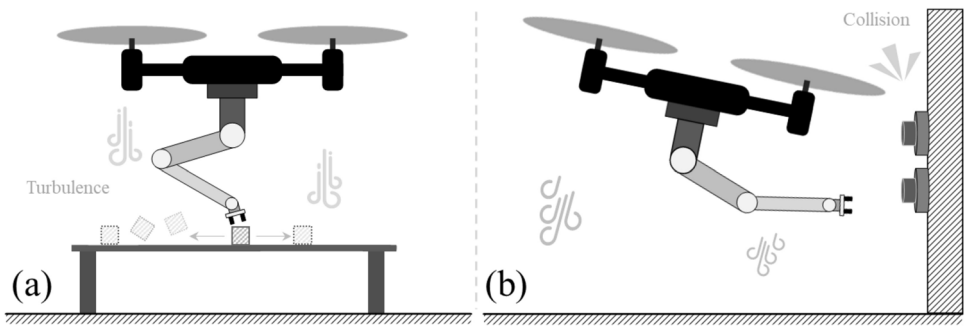

Fig. 1 (a) The downwash airflow from the propellers affects the operating target. (b) The near-wall effect for an aerial physical interaction task

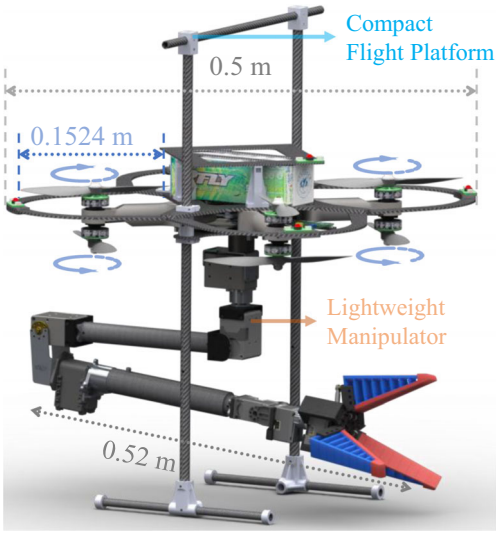

Fig. 2 The designed compact AEROM comprises a flight platform and a lightweight manipulator. The diameter of the propeller is 0.1524 m. The diagonal length of the flight platform is 0.5 m, and the manipulator length is 0.52 m with the current configuration

the skeletal structure (see Fig. 3(c) and (e)). In addition, we mount a claw equipped with three soft fingers as an end-effector for aerial dexterous operations (see Fig. 3(d)).

Moreover, the soft material fingers offer two notable advantages compared to rigid end-effectors [28–30]. The first advantage lies in the more significant coefficient of surface friction exhibited by the soft material. The second advantage arises from the natural compliance of the soft fingers with the surrounding environment. Furthermore, we incorporate a telescopic joint before the wrist joint to enhance manipulator performance, as illustrated in Fig. 3(f). The telescopic joint enables the manipulator to extend its working space without rotating joints, thus circumventing the requirement for complex kinematic solutions. Consequently, the mounted manipulator can be characterized using a set of Denavit-Hartenberg (D-H) parameters presented in Table 1.

Regarding the flight navigation and control units of AEROM, we implement these electrical units by using a hierarchical architecture, as depicted in Fig. 4, distinguishing it from conventional multi-rotors [24].

The low-level flight system incorporates a preprocessing unit that handles navigation data from sensors and remote control commands. The high-level flight system is responsible for trajectory planning, state estimation, anti-disturbance controller, and servomotor commands generation. We employ ultra wide band (UWB) wireless transmission to receive locational data from the MOCAP system. The MOCAP incorporates a UWB module, which relays the

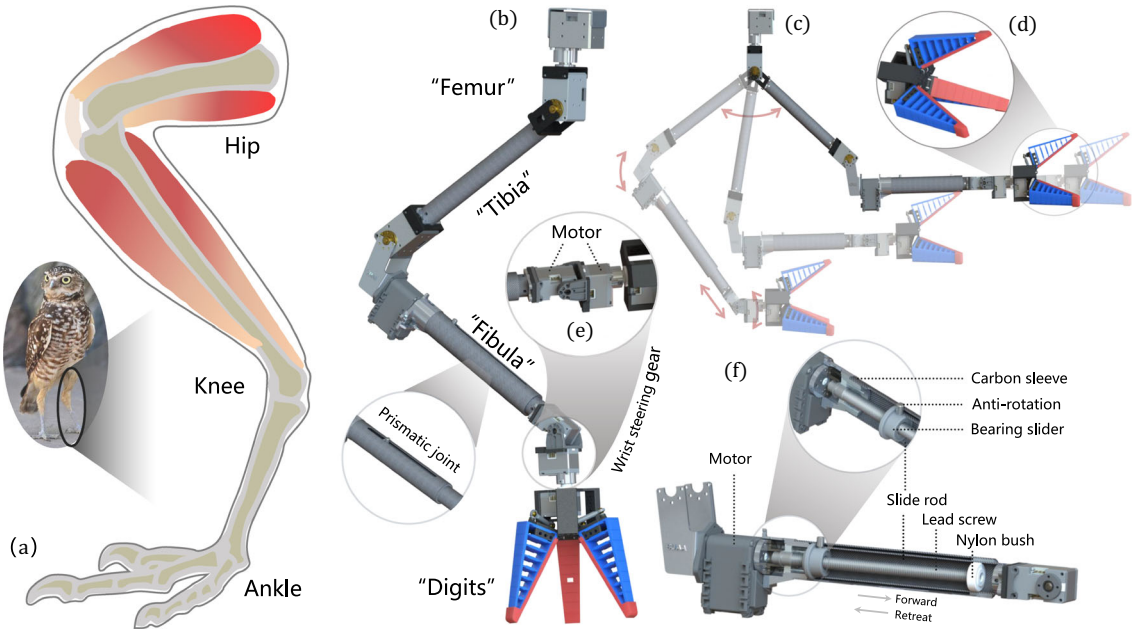

Fig. 3 The design of robotic manipulator and finger is inspired by the functional anatomy of the avian hindlimb (drawing adapted from [33]). In (a), the structure of an owl leg is shown and contrasted with the proposed manipulator in (b). (c) presents the morphology of the manipulator in different configurations. An end-effector with three soft fingers is sketched in (d). (e) and (f) represent the wrist and the prismatic joint mechanics, respectively

Table 1 The D-H parameters of manipulator

Links	θ_i [rad]	d_i [m]	α_{i-1} [m]	a_{i-1} [rad]	Offset[1] [rad]
1	q_1	0.0395	0.0	0.0	0.0
2	q_2	0.0565	0.0	$-\pi/2$	0.0
3	q_3	0.0	−0.223	0.0	$-\pi/2$
4	0.0	q_4[2]	0.038	$-\pi/2$	0.3151 [m]
5	q_5	0.0	0.0	$-\pi/2$	0.0
6	q_6	0.0423	0.0	$\pi/2$	0.0

[1]The home configuration of the manipulator
[2] The type of joint is prismatic, as shown in Fig. 3(f)

Table 2 Main physical parameters

Parameter	Value	Units
Total system mass	3.25	[kg]
Manipulator mass	0.78	[kg]
Maximum load mass	0.50	[kg]
Flight platform dimension	0.40 × 0.40 × 0.38	[m]
Diagonal distance of propulsion	0.30	[m]
Diameter of propeller	0.1524	[m]
Prismatic joint scope	0.0 ∼ 0.10	[m]
Maximum arm length	0.75	[m]
Maximum flight time	≈1000	[s]
Maximum flight speed	2.5	[m/s]
Number of servos	7	-

AEROM and the target locational data to the controller at 100 Hz.

Regarding the trajectory planner, the onboard system plans the AEROM trajectory online after it takes off. During aerial contact missions, once the trajectory planner acquires the desired end-effector path, the planner calculates the UAV position and the manipulator joint angles online according to the kinematics described in Section 3.1. Subsequently, the planner transmits the planned trajectory to the low-level controller using the serial port. Apart from the initial commands for takeoff and landing, the AEROM operates autonomously.

Finally, the onboard system is powered by a 6S-8000 mA Li-ion battery. The remaining structure of AEROM primarily comprises bespoke carbon fiber, lightweight metals, and 3D-printed components, enhancing the integrity of each module. Thus, the major system parameters are listed in Table 2.

3 Modelling of the AEROM

In this section, we model the kinematics and dynamics of the AEROM depicted above. In addition, the section describes the CoM calculation and details the proposed quantitative index to evaluate the aerial dexterity operational capability of the designed AEROM.

Let $\mathcal{F}_W$ be the inertial world-fixed frame and $\mathcal{F}_B$ be the coordinate frame attached to the geometric center of a rectangle consisting of thrusters, as shown in Fig. 5. The frames $\mathcal{F}_E$ and $\mathcal{F}_C$ are fixed to the end-effector and CoM, respectively. The direction of $\mathcal{F}_C$ is aligned with $\mathcal{F}_B$. Thus, a coordinate regarding a vector or a matrix can be denoted by a left super-

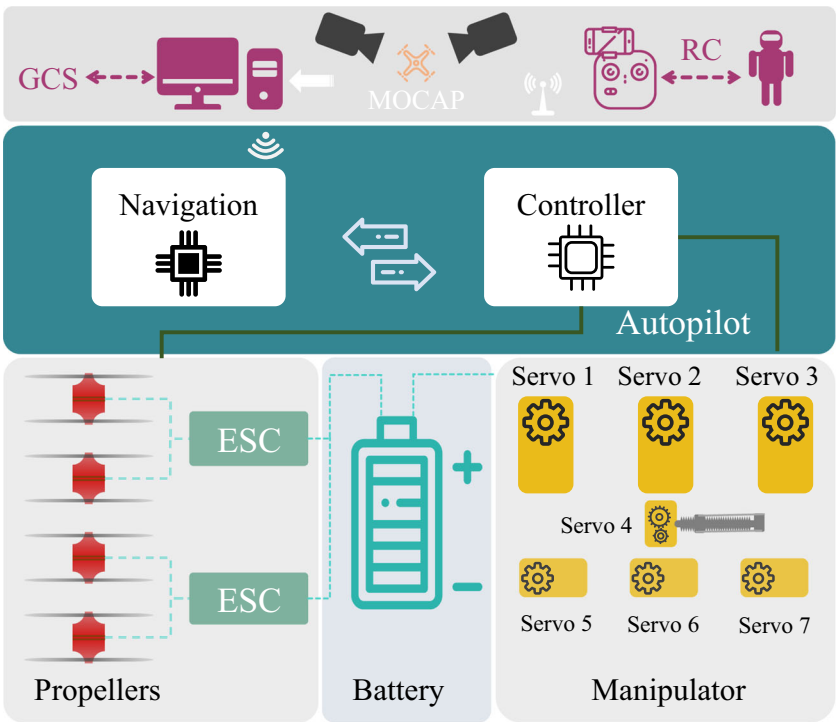

Fig. 4 The hierarchical flight system architecture for AEROM. The electronic speed controller (ESC) is responsible for controlling the propulsion system. The ground control station (GCS) transmits external localization information from a motion capture system (MOCAP) to the AEROM system. The remote control (RC) refers to the commands transmitted by a human operator through a radio control device. Note that unless unexpected incidents occur, AEROM is capable of autonomous flight without human interventions

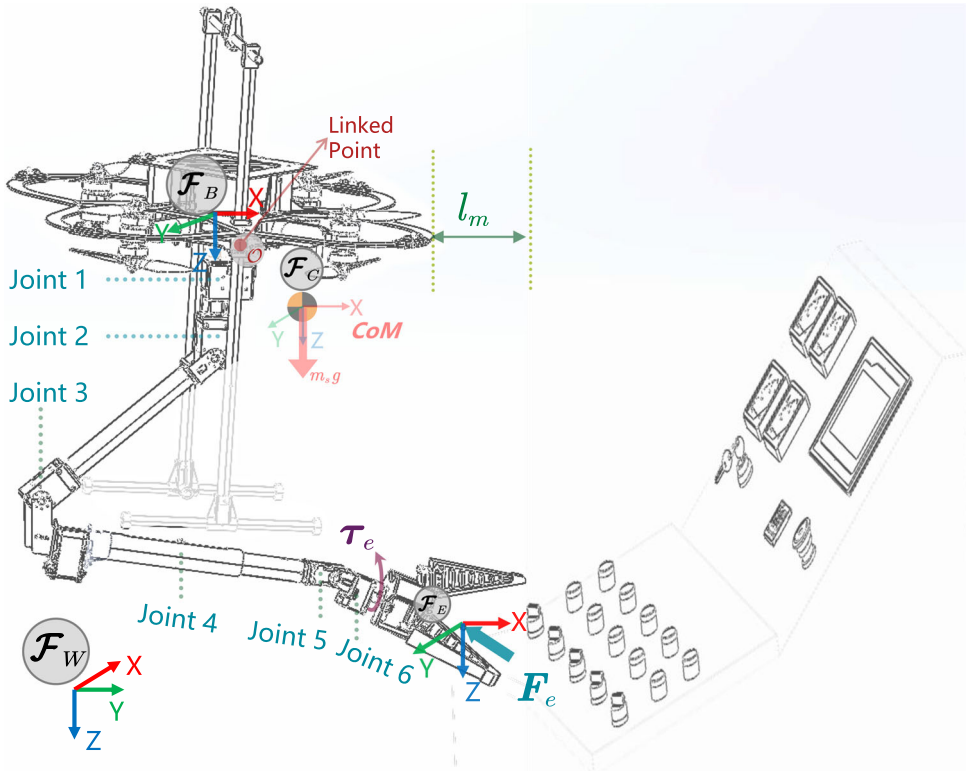

Fig. 5 The corresponding coordinate frames of the AEROM. $\boldsymbol{F}_e$ and $\boldsymbol{\tau}_e$ represent the interaction force and torque exerted on the end-effector by the surrounding environment, respectively

script. For example, ${}^{*}(A)$ expresses (A) w.r.t. the frame $\mathscr{F}_{*}$. If not specifically specified, ${}^{W}()$ will be omitted. Additionally, matrices $\boldsymbol{O}_{*}$ and $\boldsymbol{I}_{*}$ denote the zero matrix and identity matrix with appropriate dimensions, respectively. Moreover, let $\hat{*}$, $\dot{*}$, and $\ddot{*}$ represent the estimation, time derivative, and second-order derivative of $*$, respectively.

The AEROM pose is expressed by $\boldsymbol{\zeta} \in \mathbb{R}^{6+n}$ (n represents the DoF of manipulator), with the aerial vehicle position given by $\boldsymbol{P}_b \in \mathbb{R}^3$ in $\mathscr{F}_W$. The configuration of the attached manipulator is denoted as $\boldsymbol{q}_n \in \mathbb{R}^n$. The orientation of the aerial platform is given by a rotation matrix $\boldsymbol{R}_b \in \mathbf{SO}(3)$. Let $\boldsymbol{\omega}_b$ and ${}^{B}\boldsymbol{\omega}_b$ describe the angular velocities of the flight platform expressed in $\mathscr{F}_W$ and $\mathscr{F}_B$, respectively.

3.1 Forward Kinematics of the End-Effector

Let $\boldsymbol{\xi}_e = [\boldsymbol{P}_e^{\mathrm{T}} \ \boldsymbol{\eta}_e^{\mathrm{T}}]^{\mathrm{T}}$ denote the end-effector position and attitude in $\mathscr{F}_W$. The forward kinematics of end-effector can be written as:

$$\dot{\boldsymbol{\xi}}_e = \boldsymbol{T}_U(\boldsymbol{R}_b, \boldsymbol{q}_n, \dot{\boldsymbol{q}}_n) \begin{bmatrix} \dot{\boldsymbol{P}}_b \\ \boldsymbol{\omega}_b \end{bmatrix} + \boldsymbol{T}_M(\boldsymbol{R}_b, \boldsymbol{q}_n)\dot{\boldsymbol{q}}_n, \tag{1}$$

where $\boldsymbol{T}_U$ and $\boldsymbol{T}_M$ are the time-varying nonlinear functions denoting the flight platform and the manipulator kinematics, respectively. The end-effector angular velocity in $\mathscr{F}_W$ can be represented as:

$$\dot{\boldsymbol{\eta}}_e = \boldsymbol{\omega}_b + \boldsymbol{R}_b \, {}^{B}\boldsymbol{\omega}_e, \tag{2}$$

where ${}^{B}\boldsymbol{\omega}_e$ denotes the time derivative of end-effector attitude in $\mathscr{F}_B$. The linear velocity of the end-effector in $\mathscr{F}_W$ can be derived as:

$$\dot{\boldsymbol{P}}_e = \dot{\boldsymbol{P}}_b - \mathrm{Skew}(\boldsymbol{R}_b \, {}^{B}\boldsymbol{P}_e)\boldsymbol{\omega}_b + \boldsymbol{R}_b \, {}^{B}\dot{\boldsymbol{P}}_e, \tag{3}$$

where $\mathrm{Skew}(*)$ stands for the skew-symmetric matrix. Given that ${}^{B}\boldsymbol{P}_e$ represents the end-effector position in $\mathscr{F}_B$ which can be calculated using the D-H parameters in Table 1. As shown in Eqs. 2 and 3, the overall kinematics of the AEROM is composed of two portions including the UAV kinematics and manipulator kinematics. This implies an intractable coupling effect in the kinematic level.

Specifically, the attitude of the end-effector and the flight platform are interrelated due to the underactuated property of the flight platform. In order to achieve independent control of the end-effector attitude, the manipulator requires appropriate joints to decouple this attitude coupling, as shown in Fig. 3(e). This capability is crucial for achieving aerial dexterous operations.

In addition, transitioning between different manipulator configurations can lead to the AEROM mass redistribution and the CoM shift, potentially worsening oscillations of the flight platform. The oscillations can be amplified by the

manipulator joints, resulting in erosion of the end-effector performance during aerial operations.

3.2 The CoM Shift

In comparison of the free-flying before approaching the working area, the CoM shift cannot be negligible when AEROM performs dexterous aerial operations. Thus, let m_j, $\boldsymbol{P}_j$, and ${}^B\boldsymbol{P}_j$ denote the mass of link j, the CoM position of link j with respect to $\mathcal{F}_W$, and $\mathcal{F}_B$, respectively. The AEROM CoM position in $\mathcal{F}_B$ can be calculated as:

$$ {}^B\boldsymbol{P}_c = \frac{1}{m_s}\sum_{j=1}^{n} m_j\, {}^B\boldsymbol{P}_j, \tag{4} $$

where m_s represents the combined weight of AEROM, including both the flight platform and the manipulator. The CoM shift resulting from the manipulator movements will affect the flight platform from two aspects. First, the rotational inertia parameters are changed for the AEROM. Second, the manipulator movements require adequate reaction force from the connection point $\mathcal{O}$ located between the base link and the flight platform, as shown in Fig. 5. Hence, it is advisable to avoid aggressive trajectories for the manipulator joints to mitigate these effects during the aerial maneuver.

Besides, we consider the reaction force as a compensable disturbance, given partially known information (e.g., the desired trajectory of the flight platform and the manipulator). Consequently, in non-aggressive aerial dexterous operations, the reaction effects can be approximately formulated as [26]:

$$ \begin{cases} \boldsymbol{F}_l \approx -m_s\boldsymbol{R}_b({}^B\boldsymbol{\omega}_b \times ({}^B\boldsymbol{\omega}_b \times {}^B\boldsymbol{P}_c) + 2\,{}^B\boldsymbol{\omega}_b \times {}^B\dot{\boldsymbol{P}}_c) \\ \boldsymbol{\tau}_l \approx m_s({}^B\boldsymbol{P}_c \times \boldsymbol{R}_b^{-1}(g\boldsymbol{e}_3 - \dot{\boldsymbol{P}}_b)) \end{cases}, \tag{5} $$

where $\boldsymbol{e}_3$ indicates the direction of gravity. In aerial interactions, it is important to note that the end-effector experiences interaction forces, generating a deflection torque due to the CoM shift. Furthermore, the deflection torque disturbs the AEROM attitude dynamics, as explained in Section 4.2.

3.3 Quantitative Capacity of Dexterous Aerial Operations

This section analyzes the crucial factors associated with aerial dexterity manipulation. Subsequently, we propose a quantitative capability index Q_{cap} to evaluate the aerial interaction performance, as shown in Fig. 5. This index aids in the iterative optimization of the designed AEROM. The key factors encompass the flight platform compactness, the workspace of manipulator, the end-effector dexterity, and the maneuverability in targeting (e.g., the magnitude of the force exerted on the target). Thus, the quantitative index Q_{cap} is defined as:

$$ \begin{cases} I_c &= \alpha_1 \frac{l_m}{\|{}^B\boldsymbol{P}_c\|} + \alpha_2 \frac{\|\boldsymbol{F}_e^{max} - \boldsymbol{F}_e\|}{m_s g} + \alpha_3 \frac{\|\boldsymbol{\tau}_e\|}{\|\boldsymbol{\tau}_e^{max}\|} \\ Q_{cap} &= \frac{\mathrm{Rank}({}^W\boldsymbol{J}_e)}{n_{df}} \frac{V_c - V_w}{t_s\, \dot{V}_{bat}}\, e^{I_c} \end{cases}, \tag{6} $$

where the symbols physical interpretation is shown in Table 3.

A comparison between the developed AEROM and the previous work utilizing the proposed quantitative index is listed in Table 4. The AEROM designed in this study demonstrates a 62% improvement in aerial interaction capability compared to previous work [32] with $\alpha_{1,2,3} = 0.1$.

According to Eq. 6, a reduction in the AEROM mass enhances its performance. Thus, a sequential arrangement of three type servos with decreasing mass minimizes the manipulator weight, starting from the base joint to the end-effector (the mass of total servos is reduced by 35% compared to using the same servos).

3.4 The Dynamics of AEROM

Unlike conventional multi-rotor UAVs, we regard the AEROM as a solid combination of $n+1$ rigid segments in series, where n denotes DoF of the manipulator. The dynamic coupling between the flight platform and the mounted manipulator

Table 3 Nomenclature of the quantitative capability index

Symbols	Physical Interpretation
l_m	Length of the end-effector beyond propeller range[1]
${}^W\boldsymbol{J}_e$	Jacobi matrix of the forward kinematics from world to end-effector [2]
$\boldsymbol{F}_e^{max}$	The maximum force that the end-effector can exert
$\boldsymbol{\tau}_e^{max}$	The maximum torque that the end-effector can exert
$\boldsymbol{F}_e$	Interaction force actually experienced by the end-effector
$\boldsymbol{\tau}_e$	Interaction torque actually experienced by the end-effector
I_c	Temporary variable
$\alpha_{1,2,3}$	Weighting parameter, is assigned depending on the aerial mission
n_{df}	The differential flatness outputs of the flight platform [34]
V_w	Warning voltage, indicates the battery needs to be recharged
V_c	The current battery voltage, satisfying $V_c \geq V_w$
$\dot{V}_{bat}$	Battery voltage decrease rate
t_s	The flight duration time

[1] As stated in Section 2, the safety margin is contingent upon the flight platform compactness and the manipulator dimensionality

[2] The Rank of ${}^W\boldsymbol{J}_e \geqslant 6$ indicates that the end-effector position and attitude can be independently controlled regardless of the under-actuated characteristic of the flight platform

Table 4 The critical quantitative parameters of AEROM

	l_m [m]	${}^{B}P_c$ [m]	F_e^{max} [N]	m_s [kg]	τ_e^{max} [Nm]	Rank(${}^{W}J_e$)	n_{df}
This work	**0.29**	0.08	**30**	**3.25**	**0.93**	**6**	4
Previous work[1]	−0.05	0.08	22.5	3.8	0	4	4

[1] The end-effector in the previous study [32] is limited to the propellers rotation range when the manipulator is unfolded. Moreover, the previous AEROM does not include a wrist joint, which leads to the inability to exert torque on the target

presents an additional challenge for achieving aerial dexterity operations. Fortunately, studies have demonstrated that some AEROMs are differential flatness systems, where the global CoM position serves as the flat output [34, 35]. Thus, the AEROM dynamics are decoupled from the translational and postural dynamics by choosing the CoM as the coordinates frame instead of the traditional vehicle position [25]. The change of coordinates transforms the block diagonal inertia matrix, effectively decoupling the dynamics into a sparse form. Thus, the AEROM dynamics are written as:

$$\begin{bmatrix} m_s \boldsymbol{I}_3 & \boldsymbol{O}_3 \\ \boldsymbol{O}_3 & \boldsymbol{M}_r \end{bmatrix} \ddot{\boldsymbol{\xi}} + \begin{bmatrix} \boldsymbol{O}_3 & \boldsymbol{O}_3 \\ \boldsymbol{O}_3 & \boldsymbol{C}_r \end{bmatrix} \dot{\boldsymbol{\xi}} + \begin{bmatrix} \boldsymbol{G}_t \\ \boldsymbol{O}_{3+n} \end{bmatrix} = \begin{bmatrix} \boldsymbol{R}_b \boldsymbol{e}_3 & \boldsymbol{O}_3 \\ \boldsymbol{B}_r & \boldsymbol{I}_{3+n} \end{bmatrix} \boldsymbol{u} + \begin{bmatrix} \boldsymbol{F}_{dis} \\ \boldsymbol{\tau}_{dis} \end{bmatrix}, \tag{7}$$

where $\boldsymbol{\zeta} = [\boldsymbol{P}_c^{\mathrm{T}} \ \boldsymbol{\eta}_c^{\mathrm{T}} \ \boldsymbol{q}_n^{\mathrm{T}}]^{\mathrm{T}} \in \mathbb{R}^{6+n}$ is the generalized coordinate vector to constitute the system state. Specially, $\boldsymbol{P}_c$, $\boldsymbol{\eta}_c$, and $\boldsymbol{q}_n$ express the CoM position, the CoM attitude, and the manipulator configuration, respectively. Moreover, $\boldsymbol{G}_t = m_s g \boldsymbol{e}_3$ is gravity term; $\boldsymbol{u} = \left[f_t \ \boldsymbol{\tau}_c^{\mathrm{T}} \ \boldsymbol{\tau}_q^{\mathrm{T}}\right]^{\mathrm{T}}$ is system input. With respect to the system input, $f_t \in \mathbb{R}$ is the total thrust generated by the propulsion, $\boldsymbol{\tau}_c \in \mathbb{R}^3$ is the net torques around the flight platform, and the torque $\boldsymbol{\tau}_q \in \mathbb{R}^n$ is produced by the manipulator servomotors. Regarding the system mechanisms, $\boldsymbol{M}_r$, $\boldsymbol{C}_r$, and $\boldsymbol{B}_r$ denote the inertial, Coriolis, and mapping matrix that are related to rotational dynamics, respectively. Besides, $\boldsymbol{F}_{dis}$ and $\boldsymbol{\tau}_{dis}$ indicate the force and torque disturbances, respectively.

The AEROM dynamics include two cascading subsystems: the fully-actuated rotating subsystem generates the desired thrust vector to the underactuated translational subsystem. Therefore, we design the AEROM controller into two parts: one corresponds to the CoM translational dynamics, and the other to its rotational dynamics.

4 Control Method

4.1 Translational Controller

Benefited from the dynamics in Section 3.4, we choose the AEROM translation controller as follows:

$$\boldsymbol{F}_{des} = m_s \ddot{\boldsymbol{P}}_c^r + m_s g \boldsymbol{e}_3 - \boldsymbol{K}_{pc} \boldsymbol{e}_{pc} - \boldsymbol{K}_{vc} \dot{\boldsymbol{e}}_{pc} - \boldsymbol{F}_l, \tag{8}$$

where $\boldsymbol{F}_{des} = f_t \boldsymbol{R}_b \boldsymbol{e}_3 \in \mathbb{R}^3$ is the desired thrust vector, $\boldsymbol{e}_{pc}$ denotes the CoM position tracking error, and $\boldsymbol{F}_l$ is disturbance force caused by the CoM shift. Besides, $\boldsymbol{K}_{pc}$ and $\boldsymbol{K}_{vc} \in \mathbb{R}^{3\times3}$ are positive definite matrices.

Subsequently, let $\boldsymbol{F}_{des}$ project onto the body Z-axis to derive the net actual f_t and the attitude reference $\boldsymbol{R}_{des} = [\boldsymbol{b}_{1_d} \ \boldsymbol{b}_{2_d} \ \boldsymbol{b}_{3_d}] \in \mathbf{SO}(3)$ of the rotational dynamics. The thrust magnitude $f_t = \|\boldsymbol{F}_{des}\|$ and $f_t > 0$ because the AEROM will not flip over. Meanwhile, the direction of f_t is required to coincide with $\boldsymbol{b}_{3_d}$ as:

$$\boldsymbol{b}_{3_d} = \frac{\boldsymbol{F}_{des}}{\|\boldsymbol{F}_{des}\|}. \tag{9}$$

After choosing $\boldsymbol{b}_{1_d}$ from trajectory planner such that $\left\|\boldsymbol{b}_{3_d} \times \boldsymbol{b}_{1_d}\right\| \neq 0$, $\boldsymbol{b}_{2_d}$ can be derived from the following:

$$\boldsymbol{b}_{2_d} = \frac{\boldsymbol{b}_{3_d} \times \boldsymbol{b}_{1_d}}{\left\|\boldsymbol{b}_{3_d} \times \boldsymbol{b}_{1_d}\right\|}. \tag{10}$$

By combining Eqs. 9 and 10, one can obtain the desired attitude $\boldsymbol{R}_{des}$ as a referenced command for the rotational controller [35]. Note that the trajectory planning for AEROM falls outside the scope of this paper. More studies on this topic can be found in [1, 34].

4.2 Anti-disturbance Rotational Controller

According to Eq. 7, we consider the AEROM rotational dynamics as a fully actuated system and rewritten as:

$$\boldsymbol{M}_r \ddot{\boldsymbol{\eta}}_c + \boldsymbol{C}_r \dot{\boldsymbol{\eta}}_c = \boldsymbol{\tau}_c + \boldsymbol{\tau}_{dis}, \tag{11}$$

where $\boldsymbol{\eta}_c \in \mathbb{R}^3$ denotes the angular of AEROM's CoM, $\boldsymbol{\tau}_c \in \mathbb{R}^3$ is torque input from the propulsions, and $\boldsymbol{\tau}_{dis} \in \mathbb{R}^3$ denotes the system inevitable multi-source disturbances during the aerial interactive operations. Specifically, the multi-source disturbances primarily stem from three following factors:

1. Aerodynamic turbulence $\boldsymbol{f}_{dis}$, resulting from the downwash airflow and near-wall effects. The turbulence will be intensified as the AEROM approaches corners.

2. Disturbance torque $\boldsymbol{\tau}_e$, caused by the interaction which the end-effector is subjected.
3. Exogenous harmonic components $\boldsymbol{d}_{dis}$, raised from the dynamic model mismatch of AEROM, e.g., sensors measurement noise, the joints installation errors, and servomotor backlash.

According to the refined anti-disturbance control (RADC) theory [36–38], we integrate a rotational controller to compensate for or suppress the multi-source disturbances by subtly analyzing their characteristics. Therefore, $\boldsymbol{\tau}_{dis}$ can be divided into two portions:

$$\boldsymbol{\tau}_{dis} = \underbrace{\boldsymbol{\tau}_l + \boldsymbol{\tau}_e + \boldsymbol{d}_{dis}}_{\text{modeled}} + \underbrace{\boldsymbol{f}_{dis}}_{\text{unmodeled}}, \tag{12}$$

where $\boldsymbol{\tau}_l$ indicates that the modelable disturbance derives from Eq. 5, $\boldsymbol{\tau}_e = \boldsymbol{F}_e \times ({}^B\boldsymbol{P}_e - {}^B\boldsymbol{P}_c) \in \mathbb{R}^3$ denotes the torque on the CoM generated by the end-effector physical contact, $\boldsymbol{f}_{dis}$ is unmodeled but derivative-bounded disturbance (i.e., $\dot{\boldsymbol{f}}_{dis} = \boldsymbol{h}$, where $\boldsymbol{h}$ is an unknown but bounded function). In addition, $\boldsymbol{d}_{dis}$ indicates modeled harmonic component of disturbance with partially known information, which can be depicted by the following exogenous system:

$$\begin{cases} \dot{\boldsymbol{\omega}} = (\boldsymbol{W}_0 + \Delta\boldsymbol{W})\,\boldsymbol{\omega} + \boldsymbol{H}\boldsymbol{\tau}_c + \boldsymbol{d}_1 \\ \boldsymbol{d}_{dis} = \boldsymbol{V}\boldsymbol{\omega} \end{cases}, \tag{13}$$

where $\boldsymbol{\omega}$ is a selected state variable according to the disturbance priori model, $\boldsymbol{W}_0$ is nominal model of exogenous harmonic components, $\Delta\boldsymbol{W}$ is the bounded uncertainty of the disturbance model, $\boldsymbol{H}$ and $\boldsymbol{V}$ denote the disturbance priori knowledge. Note that $\boldsymbol{d}_1$ is an auxiliary variable.

The multi-source disturbances in Eq. 12 can be classified into two categories: the first category comprises the modeled disturbances (i.e., $\boldsymbol{\tau}_l$, $\boldsymbol{\tau}_e$, and $\boldsymbol{d}_{dis}$), while the second category consists of the unmodeled derivative-bounded disturbance $\boldsymbol{f}_{dis}$. Therefore, combining the model-based disturbance observer (DO) with an extended state observer (ESO) enables simultaneous suppression of both $\boldsymbol{d}_{dis}$ and $\boldsymbol{f}_{dis}$ [38].

Let $\boldsymbol{x}_1 = \boldsymbol{\eta}_c$ and $\boldsymbol{x}_2 = \dot{\boldsymbol{\eta}}_c$ denote the angle and angular velocity vector of AEROM CoM, respectively, and $\boldsymbol{x}_3 = \boldsymbol{f}_{dis}$. The AEROM rotational dynamics Eq. 11 can be rewritten as:

$$\begin{cases} \dot{\boldsymbol{x}}_1 = \boldsymbol{x}_2 \\ \dot{\boldsymbol{x}}_2 = \boldsymbol{M}_r{}^{-1}(-\boldsymbol{C}_r\boldsymbol{x}_2 + \boldsymbol{\tau}_c + \boldsymbol{x}_3 + \boldsymbol{d}_{dis}) \\ \dot{\boldsymbol{x}}_3 = \boldsymbol{h}_{dis} \end{cases} \tag{14}$$

where $\boldsymbol{x}_1$ and $\boldsymbol{x}_2$ are measured from onboard sensors (e.g., inertial measurement unit). Subsequently, let $\boldsymbol{y} = \begin{bmatrix} \boldsymbol{y}_1 \\ \boldsymbol{y}_2 \end{bmatrix} = \begin{bmatrix} \boldsymbol{x}_1 + \boldsymbol{v}_1 \\ \boldsymbol{x}_2 + \boldsymbol{v}_2 \end{bmatrix}$ represent the measurement outputs of Eq. 11, where the measurement bias $\boldsymbol{v} = [\boldsymbol{v}_1^{\mathrm{T}} \ \boldsymbol{v}_2^{\mathrm{T}}]^{\mathrm{T}}$ and its derivative $\dot{\boldsymbol{v}}$ are assumed to be bounded [38]. Thus, an disturbance observer can be designed for $\boldsymbol{d}_{dis}$ as:

$$\begin{cases} \hat{\boldsymbol{d}}_{dis} = \boldsymbol{V}\hat{\boldsymbol{\omega}} \\ \hat{\boldsymbol{\omega}} = \boldsymbol{\Gamma} + \boldsymbol{L}\boldsymbol{M}_r\boldsymbol{y}_2 \\ \dot{\boldsymbol{\Gamma}} = (\boldsymbol{W}_0 - \boldsymbol{L}\boldsymbol{V})\,\hat{\boldsymbol{\omega}} + (\boldsymbol{H} - \boldsymbol{L})\,\boldsymbol{\tau}_c - \boldsymbol{L}\boldsymbol{z} \\ \boldsymbol{z} = -\boldsymbol{C}_r\hat{\boldsymbol{x}}_2 + \hat{\boldsymbol{x}}_3 \end{cases} \tag{15}$$

where $\boldsymbol{L}$ is the gain matrix, $\boldsymbol{\Gamma}$ and $\boldsymbol{z}$ are auxiliary variables.

In order to estimate the remaining unmodeled disturbance $\boldsymbol{f}_{dis}$, we construct an ESO as follows by utilizing the DO output:

$$\begin{cases} \dot{\hat{\boldsymbol{x}}}_1 = \hat{\boldsymbol{x}}_2 + \boldsymbol{K}_1\left(\boldsymbol{y} - \hat{\boldsymbol{y}}\right) \\ \dot{\hat{\boldsymbol{x}}}_2 = \boldsymbol{M}_r{}^{-1}\left(\boldsymbol{z} + \boldsymbol{\tau}_c + \hat{\boldsymbol{d}}_{dis}\right) + \boldsymbol{K}_2\left(\boldsymbol{y} - \hat{\boldsymbol{y}}\right), \\ \dot{\hat{\boldsymbol{x}}}_3 = \boldsymbol{K}_3\left(\boldsymbol{y} - \hat{\boldsymbol{y}}\right) \end{cases} \tag{16}$$

where $\boldsymbol{K}_1$, $\boldsymbol{K}_2$ and $\boldsymbol{K}_3$ are the gain matrices of the ESO.

In summary, by combining the DO and ESO, one can integrate the RADC as:

$$\begin{aligned} \boldsymbol{\tau}_c = & \underbrace{-\boldsymbol{K}_{rp}\boldsymbol{e}_\eta - \boldsymbol{K}_{rd}\boldsymbol{e}_\omega}_{\text{feedback}} + \underbrace{\boldsymbol{M}_r\dot{\boldsymbol{\omega}}_d + \boldsymbol{C}_r\boldsymbol{\omega}_d}_{\text{feedforward}} \\ & \underbrace{-\hat{\boldsymbol{d}}_{dis} - \hat{\boldsymbol{f}}_{dis} - \boldsymbol{\tau}_e - \boldsymbol{\tau}_l}_{\text{compensation}} \end{aligned} \tag{17}$$

where $\boldsymbol{e}_\eta = \frac{1}{2}(\boldsymbol{R}_{des}^{\mathrm{T}}\boldsymbol{R}_b - \boldsymbol{R}_b^{\mathrm{T}}\boldsymbol{R}_{des})^\vee$ indicates the attitude tracking error. [1] The gain matrices $\boldsymbol{K}_{rp}$ and $\boldsymbol{K}_{rd}$ are positive definite matrices. The angular velocity error $\boldsymbol{e}_\omega$ is represented in CoM frame and is given by $\boldsymbol{e}_\omega = \boldsymbol{\omega}_b - \boldsymbol{\omega}_d$, where $\boldsymbol{\omega}_d = \boldsymbol{R}_b^{\mathrm{T}}\boldsymbol{R}_{des}(\boldsymbol{R}_{des}^{\mathrm{T}}\dot{\boldsymbol{R}}_{des})^\vee$. Besides, given that desired angular acceleration $\dot{\boldsymbol{\omega}}_d$ in the feedforward term represents the derivative of $\boldsymbol{\omega}_d$, we employ a filter (i.e., tracking differentiator) to obtain $\dot{\boldsymbol{\omega}}_d$.

Figure 6 illustrates the control architecture of the proposed AEROM system. Subsequently, we conduct a series of physical experiments to assess the effectiveness of the deployed RADC on the AEROM. In control allocation for AEROM actuators, we distinguish between motors and servos due to their different features. A conventional quadcopter

[1] The vee operator $(*)^\vee$ a is the inverse of the hat operator, which is defined by $\boldsymbol{a} \times \boldsymbol{b} = \hat{\boldsymbol{a}}\boldsymbol{b}$.

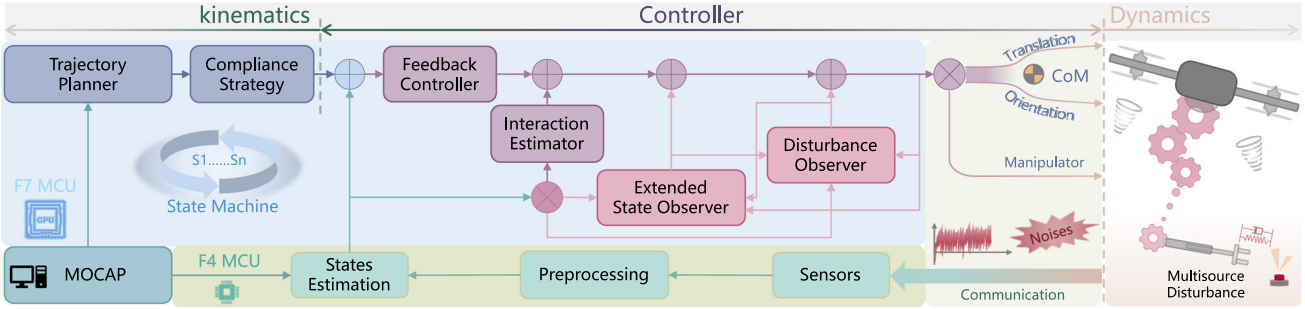

Fig. 6 The control architecture of the proposed AEROM system. Note that a motion capture system (MOCAP) is employed to perceive the position information

motor mapping is used for flight [24], while a 1000 Hz PID controller maintains each servo performance [32].

5 Physical Experiments

In this section, we conduct four experiments to verify the capabilities of the proposed AEROM system. First, we verify the dexterity of end-effector throughout a ground test, whose attitude error can be compensated by the designed manipulator independently of the UAV. Second, the AEROM performs a set of flight experiments to assess the effectiveness of the proposed RADC. Third, the experiment involving the aerial grabbing and placement of an egg showcases the AEROM precise maneuverability. Lastly, the AEROM manipulates a button to exhibit its aerial dexterity during physical interaction. Moreover, we utilize the mean absolute error (MAE) and root mean square error (RMSE) to facilitate quantitative analysis. The MAE and RMSE are defined as $MAE = \frac{1}{n_d}\sum_{i=1}^{n_d} \| \boldsymbol{x}_i - \boldsymbol{x}_{d,i} \|$, $RMSE = \sqrt{\frac{1}{n_d}\sum_{i=1}^{n_d} \| \boldsymbol{x}_i - \boldsymbol{x}_{d,i} \|^2}$ where n_d is the number of collected data, $\boldsymbol{x}_i$ and $\boldsymbol{x}_{d,i}$ are i-th actual variable and its desired value. The experimental videos can be found at https://youtu.be/ZoRAhNFOD80.

5.1 Ground Test of the End-effector Dexterity

Scenario Setup The experiment involves artificially shaking the UAV while requiring the end-effector to maintain a fixed attitude, as depicted in Fig. 7. To maintain the end-effector attitude, the manipulator utilizes joints 1, 5, and 6 (see Fig. 5) to compensate for yaw, pitch, and roll error, respectively, when the UAV is shaken artificially. In this scenario, a mini laser fixed to the claw emits a red cross, which indicates the claw attitude. Furthermore, an external motion capture system (MOCAP) provides the UAV attitude information. An additional IMU installed at the end-effector records the end-effector attitude changes when the UAV is artificially shaken. Note that the autopilot autonomously plans the manipulator joints movements without human instructions. Figure 8 displays the experimental results.

Result and Analysis As illustrated by the shading in Fig. 8(a), although the UAV yaw peaks at 0.665 rad ($t \approx 46$s), the end-effector heading is approximately unchanged (peak of -0.0389 rad). This implies that the joint 1 can counteract the UAV yaw variation, thereby maintaining a nearly constant heading for the end-effector. Similar pitch and roll angle observations are also found in Fig. 8(b) and (c). Therefore,

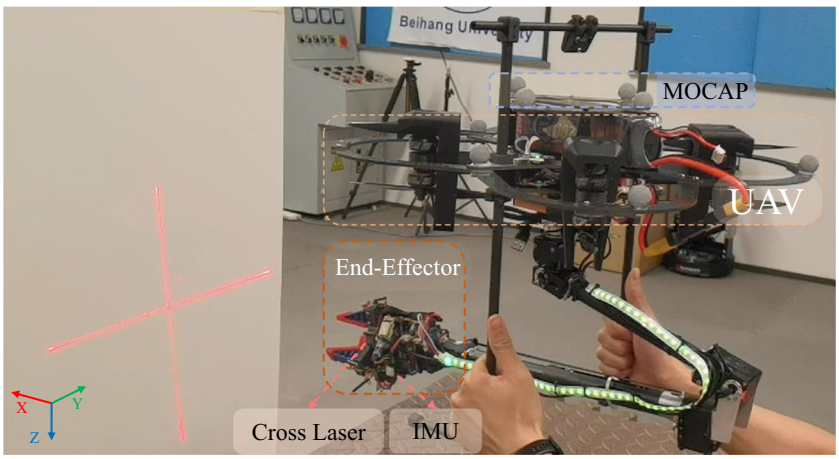

Fig. 7 The setup of ground test. The UAV is artificially shaken during the experiment. Simultaneously, the MOCAP and additional IMU recorded the attitude variations of the UAV and the end-effector, respectively

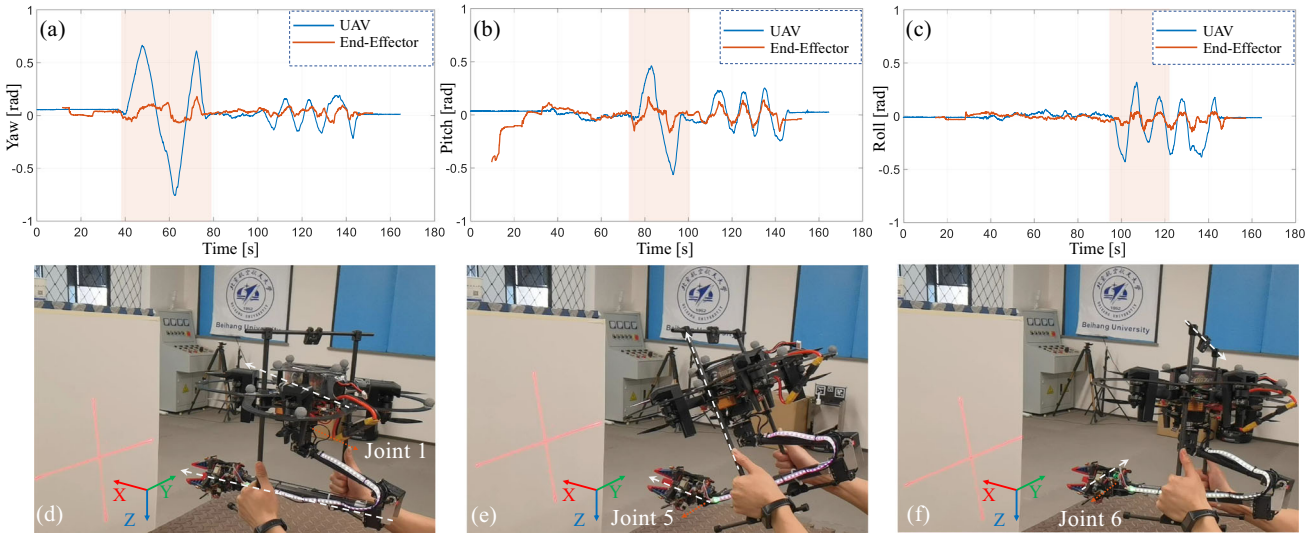

Fig. 8 Ground test results of the end-effector dexterity. From (a) and (d), joint 1 compensates for the yaw deviation when deflected the UAV heading. (b) and (e) demonstrate joint 5 canceling out the UAV pitch bias. (c) and (f) illustrate that joint 6 counters the effect of the UAV roll on the end-effector

the designed manipulator can effectively employ its joints to compensate the impact of UAV attitude changes on the end-effector.

Table 5 lists the corresponding statistical results, including the range of attitude changes and the mean values. The range of attitude change for the end-effector is reduced by 79.3%, 75.3%, and 72.2% in yaw, pitch, and roll, respectively, compared to the UAV. Regarding the MAE, the end-effector attitude relative to the UAV shows a decrease of 78.62% in yaw, 66.14% in pitch, and 53.71% in roll. In addition, the comparison using RMSE also indicates that the end-effector attitude distribution is more concentrated than the UAV.

The combination of Fig. 8 and Table 5 demonstrates that the end-effector attitude can be independently controlled regardless of the UAV, which is crucial for aerial dexterous operations. The results demonstrate the efficacy of the manipulator, which is designed utilizing the quantitative index proposed in Section 3.3. Thus, our AEROM holds a Rank($^W\boldsymbol{J}_e$) of 6, which is deemed to be good. Otherwise, in a context where a Rank($^W\boldsymbol{J}_e$) of 5 signifies an average status, while a rank of 4 is seen as poor.

5.2 Trajectory Tracking without Contact

Scenario Setup In this scenario, we test the AEROM by following a circular trajectory to assess the effectiveness of the designed control architecture, as illustrated in Fig. 9. Moreover, to showcase the RADC performance presented in Section 4, we utilize a nominal controller [32] without RADC as a baseline for comparison. The trajectory tracked $\boldsymbol{P}_{bd} = \left[P_{dx}, P_{dy}, P_{dz}\right]^{\mathrm{T}}$ is described as following:

$$\begin{cases} p_{dx} = 1 * \sin\left(0.4\pi t\right) \\ p_{dy} = -1 * \cos\left(0.4\pi t\right) \\ p_{dz} = -1.2 \end{cases}, \tag{18}$$

where t is flight time. The mounted manipulator is torqued and unfolded before the UAV tracks the trajectory. During the contactless flight, we configure the manipulator joints to the constant values as $\boldsymbol{q}_{cf} = [0, -\pi/6, \pi/6, 0, 0, 0]^{\mathrm{T}}$. Furthermore, the trajectory planner generates tracked trajectories using the predefined functions in Eq. 18.

Table 5 Attitude changes of the UAV and end-effector (EEF)

	Yaw [rad]			Pitch [rad]			Roll [rad]		
	PR[1]	MAE	RMSE	PR	MAE	RMSE	PR	MAE	RMSE
UAV	1.4242	0.3050	0.3825	1.0257	0.2555	0.3097	0.7507	0.1871	0.2221
EEF	0.2944	0.0652	0.0737	0.2531	0.0865	0.1026	0.2083	0.0866	0.0996

[1]Note: The peak range (PR) represents the extent of attitude changes

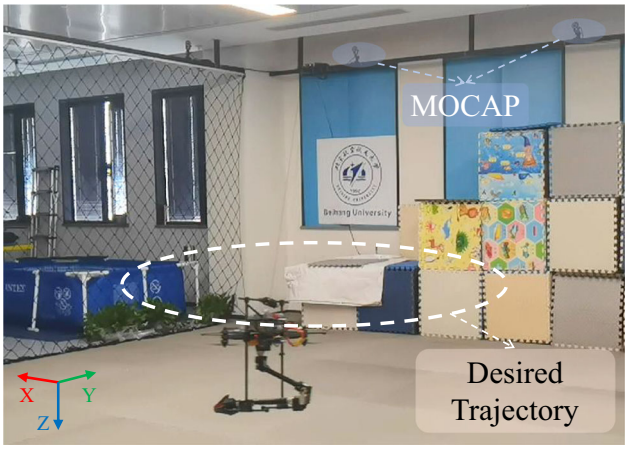

Fig. 9 The scenario of trajectory tracking. The white dashed line indicates the UAV desired trajectory. The MOCAP provides the localization information for the AEROM

Experimental Results Figure 10 shows the results of the flight comparison. It can be observed that AEROM can track the desired trajectory efficiently. Thus, the system architecture in Section 2 is effective. Additionally, Table 6 presents the statistical results for comparing trajectory tracking performance between the RADC and baseline methods. Table 6 indicates the Y-axis tracking error RMSE is higher than the X and Z-axes using a baseline controller without RADC. This implies a wider spread in Y-axis tracking errors, signifying less precision in trajectory tracking on the Y-axis compared to the X and Z-axes. As discussed in Section 3.2, the discrepancy can be attributed to the extension of the manipulator, which primarily impacts the CoM shift in the X and Z axes.

Analysis and Discussion Moreover, the statistical analysis in Table 6 indicates a 8.38% increase in trajectory tracking accuracy compared to the baseline. The reduction in the MAE of the tracking error reflects this improvement. The improvement does not seem significant because there is not much disturbance in this scenario. However, the impact of disturbances will be more significant when the AEROM performs aerial operation missions, as opposed to the situation without contact during free flight. Consequently, the performance of RADC for the AEROM is higher, as shown in the subsequent aerial interaction experiment.

5.3 Aerial Grabbing and Placing

Scenario Setup In this scenario, we assign the AEROM to pick up an egg (maximum diameter ≈ 4 cm) and place it into a cup (diameter ≈ 7 cm), as illustrated in Fig. 11. Additionally, we implement a priority-based hierarchical approach to system redundancy, which encompasses control of the end-effector position and orientation, as well as the CoM management. The aerial grabbing task includes the following steps.

Initially, the AEROM approaches the designated target after takeoff and initializing the manipulator (see Fig. 11(a)). Subsequently, the mounted manipulator actuates the joints to orient the end-effector towards the targeted egg (see Fig. 11(b)). Upon grasping the egg, the AEROM moves towards the cup and accurately places the egg (see Fig. 11(c)). After the task has been accomplished, the manipulator joints are reset to the home configuration. Figure 12 illustrates the trajectory of the AEROM during the aerial grasping task. It should be emphasized that AEROM operates autonomously throughout the entire mission. The autopilot generates the flight platform trajectory and the manipulator joints command online, with the locations of the egg and the cup having been determined via the MOCAP.

Experimental Process and Difficulties It is observed that the AEROM trajectory tracking accuracy during maneuvering is worse (see green shading in Fig. 12) compared to hovering (see blue shading in Fig. 12), especially in the Y-axis. This is because the CoM shift caused by the mounted manipulator impairs the position transient response of the AEROM, as analyzed in Section 3.2. In addition, Fig. 12(d) demonstrates that the manipulator unfolding and the egg grabbing induce the AEROM position fluctuations, potentially leading to the aerial task failures. Within the scope of our study, we catego-

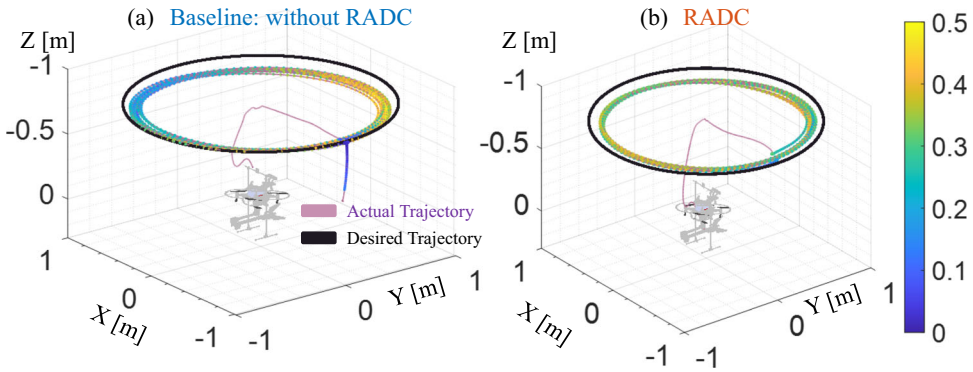

Fig. 10 AEROM trajectory data for 3D points, colored by the norm of position tracking error. (a) and (b) illustrate the UAV using the baseline and RADC approaches, respectively. The black solid line is the desired trajectory, while the colored dashed line represents the actual position

Table 6 Statistical results of trajectory tracking comparison

	MAE [m]			RMSE [m]			
	X	Y	Z	X	Y	Z	
With RADC	0.0267	0.0263	0.0154	0.0572	0.0575	0.0635	↑**8.38%**
Baseline: without RADC	0.0321	0.0339	0.0198	0.0623	0.0663	0.0659	

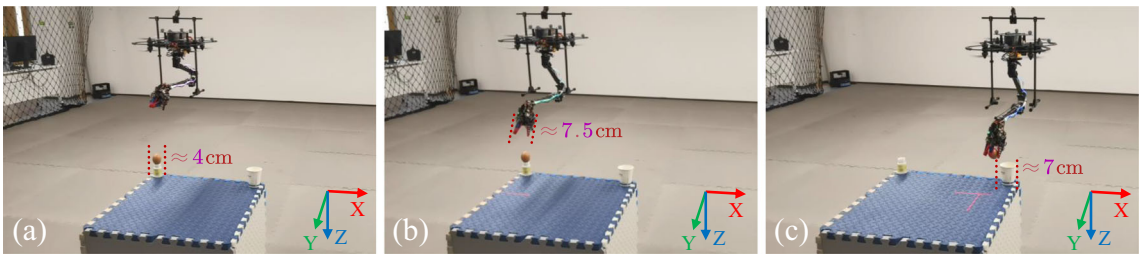

Fig. 11 Aerial grabbing of an egg and placing it in a cup. (a) The AEROM is approaching the target. (b) The manipulator has been extended to facilitate the target grab. (c) The egg is transferred over the cup and carefully placed. Note: The fragile egg remains undamaged throughout the aerial grab

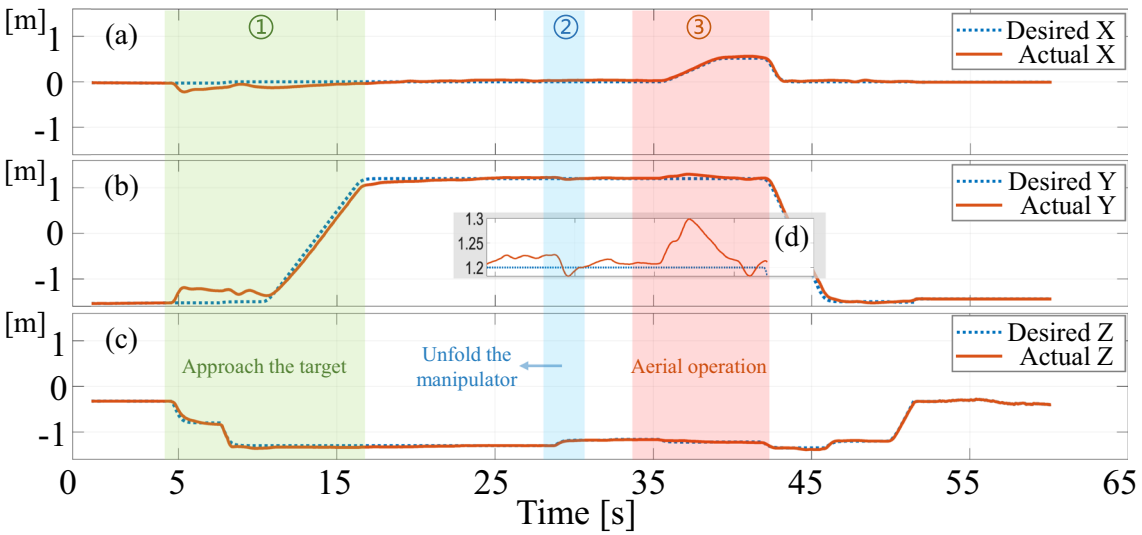

Fig. 12 The position of AEROM changes during the aerial egg grasping. (a), (b), and (c) illustrate the AEROM position along the X, Y, and Z axes, respectively. (d) provides zoomed-in details of the corresponding variable changes. Circle numbers ①, ②, and ③ indicate the stages of approaching the target, unfolding the manipulator, and aerial operating the egg, respectively

Table 7 Comparison results in the aerial grabbing scenario

	Category	MAE [m]	RMSE [m]	Success Rate
With RADC	Grab egg	0.0456	0.0492	**80%**
	Drop egg	0.0494	0.0565	**80%**
Baseline: without RADC	Grab egg	0.0761	0.0947	60%
	Drop egg	0.0669	0.0859	40%

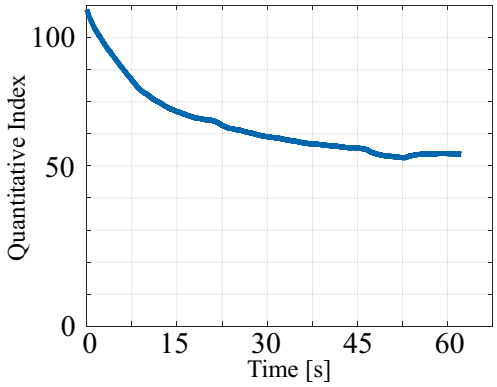

Fig. 13 Variation in quantitative index in the aerial grabbing and placing of an egg task

rize incidents such as missing the egg, missing the designated cup, and dropping the egg as indicative of task failure.

Results and Discussion Despite these challenges, the deployed RADC exhibits satisfactory trajectory accuracy, enabling the AEROM to accomplish the task (see Fig. 11). Table 7 presents the tracking error statistics of the RADC and the baseline controller in the given scenario. Note that the tracking error evaluation refers to the end-effector position, which is crucial for successful aerial grabbing and placement tasks. The deployed RADC exhibits enhanced positional accuracy relative to the baseline. Furthermore, the statistics indicate a more centralized distribution of the RADC, as evidenced by the lower RMSE. Thus, the RADC exhibits an 33.57% improvement in performance by effectively reducing the MAE of the tracking error.

Additionally, each controller undergoes five repetitive aerial grabbing tasks, and their respective success rates are recorded in Table 7. We divide the aerial egg retrieval challenge into two components: grabbing and placing. The proposed RADC enhances AEROM grabbing egg success rate by 20% (from 60% to 80%). Regarding egg placement, RADC doubles the baseline success rate from 40% to 80%.

The results in Fig. 12 and Table 7 confirm that the designed AEROM system can operate the fragile target from the air.

Considering the quantitative indicators described in Eq. 6, Fig. 13 illustrates the evolution of the index. It is important to recognize that the choice of hyperparameters significantly affects the values obtained from the quantitative index. In this scenario, the chosen settings enable us to define performance benchmarks: a quantitative index above 80 is deemed excellent, and below 35 is regarded as substandard. A score between 35 and 80 indicates a moderate performance.

5.4 Aerial Operation of a Push Button

Scenario Setup In this scenario, AEROM is operating a button (≈ 4 cm) on an industrial cabinet to evaluate its capability for dexterous aerial operations under multiple source disturbances, as illustrated in Fig. 14(a). The dimension of the cabinet is 0.60 m $\times$ 0.57 m $\times$ 1.25 m. We install an additional two-color indicator light on the cabinet to show the status (green indicates unlocked and red locked). The solid yellow line in Fig. 14(b) depicts the AEROM trajectory during the aerial operation task. It is worth noting that the AEROM operates the button autonomously during the flight without human interventions.

Mission Stages The task involving the operation button consists of four distinct phases. During the initial stage, as depicted in Fig. 15(a), the AEROM ascends from the ground to a specified altitude. Subsequently, the AEROM undergoes unrestricted flight towards the industrial cabinet, as illustrated in Fig. 15(b). The third stage involves the UAV hovering above the target (see Fig. 15(c)). The manipulator activates the end-effector to establish physical contact and depress the button. As a response, the indicator light changes from green to red. Upon completing the aerial operational task, the AEROM returns to the origin and retracts the manipulator to the home configuration, as depicted in Fig. 15(d).

Experimental Results Figure 16 illustrates the critical variables during the flight, including the AEROM position and yaw. The UAV performs a 90-degree right-angle turn after

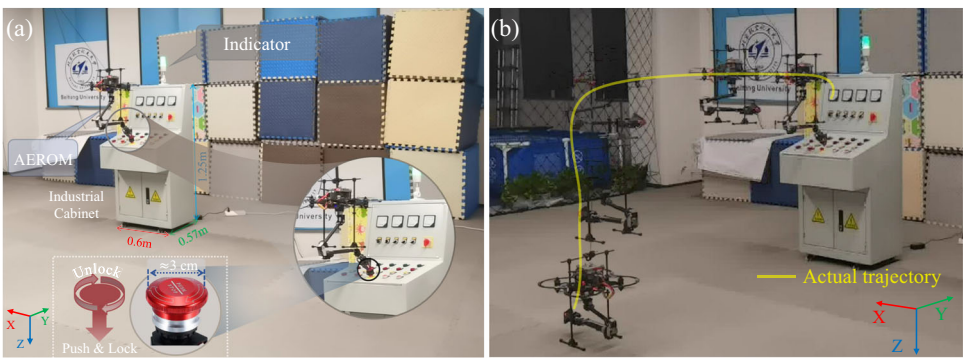

Fig. 14 The AEROM is operating a button of an industrial cabinet. (a) The indicator located on top of the cabinet shows the status of the button. (b) The yellow line represents the AEROM flight trajectory captured through snapshots. Note that the AEROM aerial operation of a button is performed autonomously

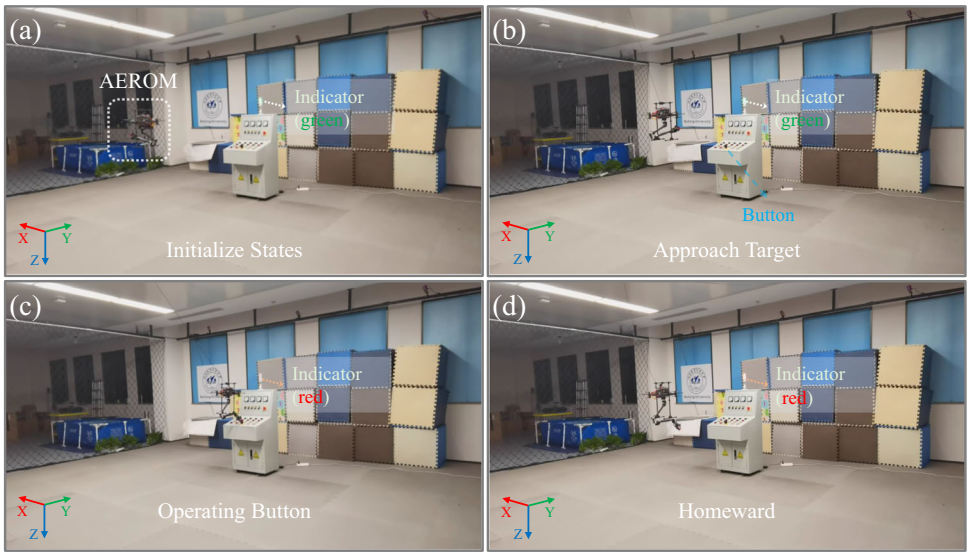

Fig. 15 Experimental snapshots of aerial operation button. (a) Initialize states: The AEROM takes off from the ground to a specified altitude and acquires the button position. (b) Approach target: The AEROM flights toward the control cabinet. (c) Operating button: The UAV hovers at an appropriate position above the target. The manipulator drives the end-effector to establish physical contact with the button surface and push down the button. (d) Homeward: After completing the aerial operation, the AEROM returns to the origin and landing

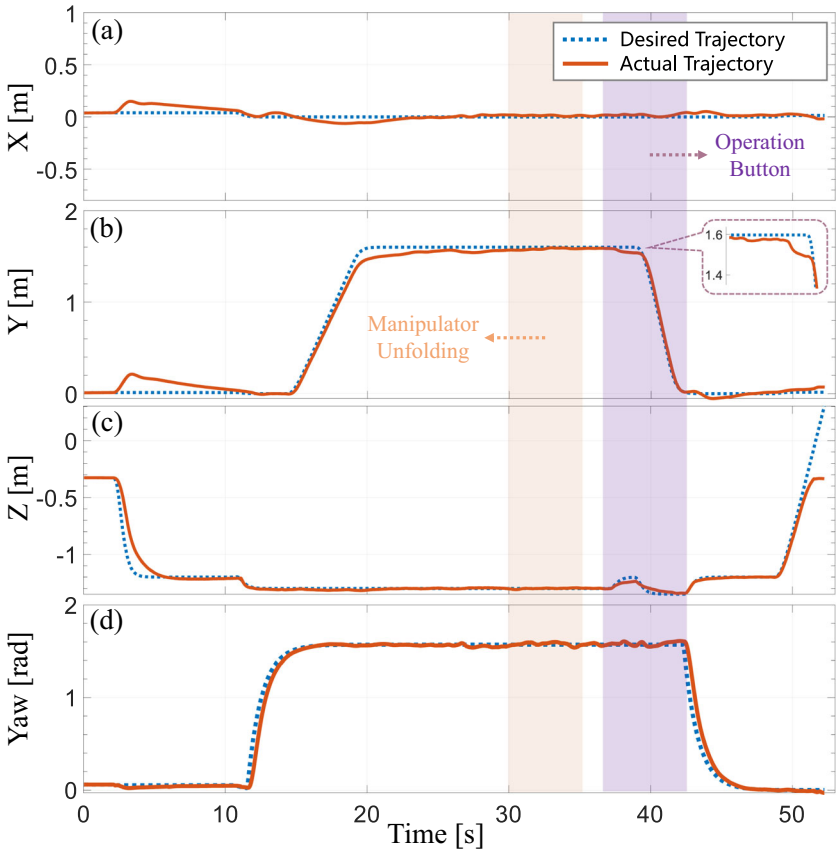

Fig. 16 The actual and desired trajectory of AEROM during operation button. (a)-(d) represent the variation in AEROM position and yaw angle throughout the flight, respectively. The yellow shading signifies the manipulator is unfolding, and the purple indicates the button operation

Table 8 Comparison results in the push button scenario

	MAE [m]			RMSE [m]			
	X	Y	Z	X	Y	Z	
With RADC	0.0348	0.0512	0.0349	0.0617	0.1000	0.1220	↑**32.69%**
Baseline: without RADC	0.1010	0.1282	0.0582	0.1240	0.1551	0.1424	

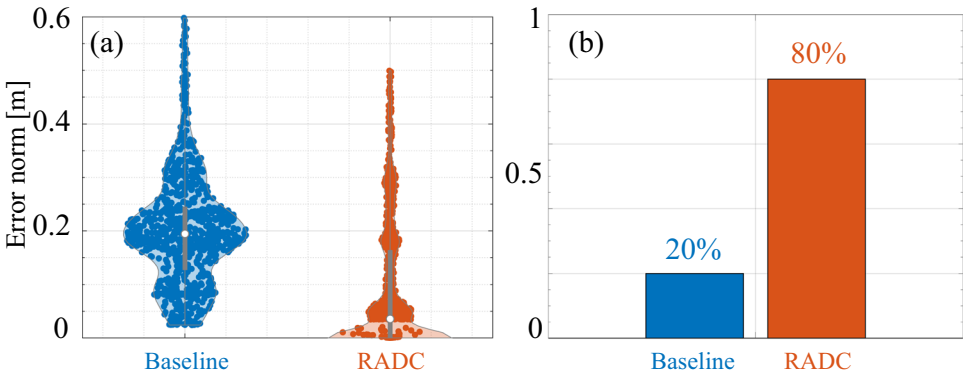

Fig. 17 (a) The violin plot of the tracking error distribution of the baseline and RADC. (b) The success rate of aerial push-button operation

takeoff, allowing the end-effector to align with the button, as shown in Fig. 16(d). The yellow shading represents the influence of manipulator motions on the AEROM position, while the purple shading represents the influence of the operation button. This is attributed to the impact of the CoM shift and external physical interactions. However, the deployed RADC ensures the AEROM positional accuracy during the aerial operation button.

Consequently, Table 8 lists statistical analysis of the flight data collected during aerial operations to validate the AEROM performance. The flight data primarily comprises the end-effector position, which is the focus of the AEROM in this study. Compared to the baseline, the trajectory tracking performance of RADC shows a 32.69% improvement in the RMSE of the tracking error. This improvement demonstrates the effectiveness of RADC in enhancing trajectory tracking accuracy.

Analysis and Discussion To further demonstrate the advantages of RADC, Fig. 17(a) presents an additional violin plot to illustrate the distribution of AEROM position error. The RADC exhibits a more concentrated position error distribution than the baseline. This helps to improve the success rate of AEROM in accomplishing aerial dexterity operations.

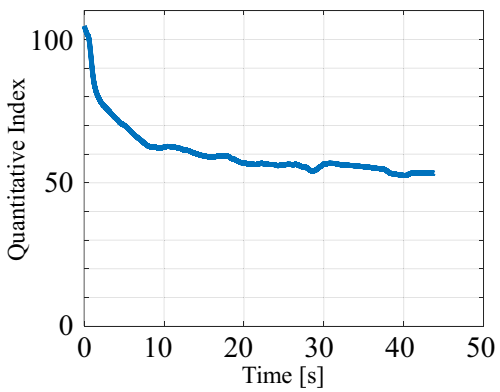

Fig. 18 Variation of the quantitative index during the aerial button operation

Next, ten repetitive experiments are conducted to compare the task success rates of the baseline and RADC. The results shows that the success rate of the aerial button operation is increased from 20% to 80%, as shown in Fig. 17(b). This demonstrates that the RADC assists the AEROM in mitigating the disturbances caused by manipulator motions and turbulence during aerial dexterous operations.

Regarding the quantitative index, Fig. 18 depicts the variation of the index. In this task, our criteria classify a quantitative index above 80 as excellent and below 35 as poor, with $35 \sim 80$ reflecting average performance.

Lastly, Fig. 19 displays the controller outputs (desired thrust and attitude torque). As shown in the red shading of Fig. 19, the fluctuation in the controller output exhibits that the AEROM is struggling with external interaction. Thanks to the deployed RADC, the end-effector maintains stable contact with the button throughout the aerial task execution. This validates that the AEROM designed in this work effectively performs aerial dexterous operations.

Furthermore, we have observed an attractive phenomenon regarding the desired thrust uncertainty. Specifically, although the AEROM has a total weight of 3.25 kg, the desired thrust of the controller is approximately 40 N. The diminished thrust may be attributed to the reduced propeller aerodynamics due to the coaxial rotor configuration, even though this configuration improves the load capacity of the AEROM. Hence, analysis and compensation for the thrust uncertainty is one of our future works.

6 Conclusions

In this work, we present an AEROM prototype for dexterous aerial operations that require physical interaction, such as industrial cabinet operations. Advantages of this study include: 1) we introduce a quantitative capability index for AEROM evaluation, which guides the AEROM design and performance assessment; 2) our study presents a compact AEROM with a multirotor and a lightweight bio-inspired

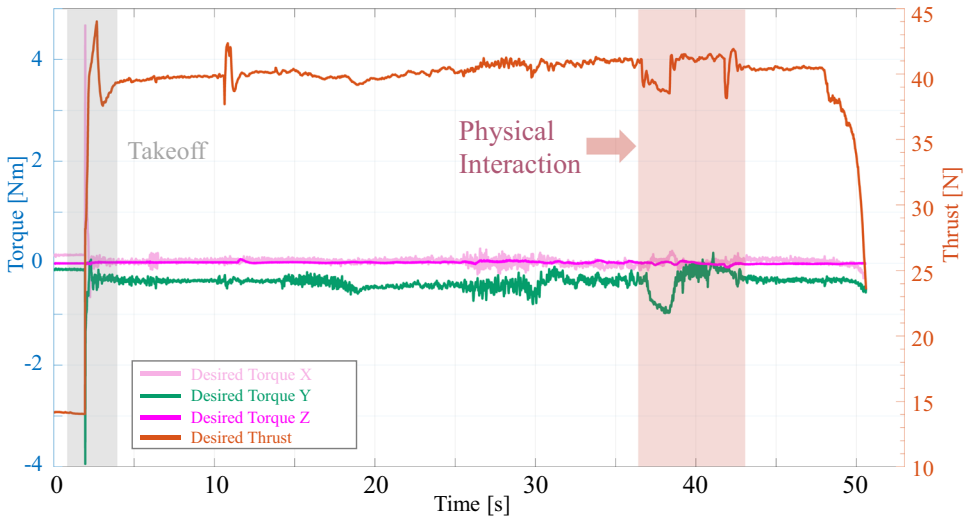

Fig. 19 The controller outputs of the UAV. The gray (left) and red (right) shading indicate that the UAV is in the takeoff and environment interaction stages, respectively

manipulator that ensures precise end-effector operation with independent position and orientation control; and 3) we employ a refined anti-disturbance controller (RADC) to enhance flight stability with multi-source disturbances (i.e., interaction force, external turbulence, the CoM shift, and the joint motion error). These advantages improve the performance of AEROMs during physical interactions. Finally, several physical experiments validate the effectiveness of the proposed AEROM system, such as aerial grabbing egg and operation of the button.

Author Contributions Conceptualization: Qianyuan Liu, Kexin Guo, Xiang Yu, and Lei Guo; methodology: Qianyuan Liu, Kexin Guo, and Xiang Yu; software: Qianyuan Liu and Zeshuai Chen; validation: Qianyuan Liu, Yuhang Liu, and Zeshuai Chen; formal analysis: Qianyuan Liu, Kexin Guo, and Xiang Yu; investigation: Qianyuan Liu, Kexin Guo, and Xiang Yu; writing original draft preparation: Qianyuan Liu, Kexin Guo, Xiang Yu, and Youmin Zhang; writing review and editing: Qianyuan Liu, Kexin Guo, Xiang Yu and Youmin Zhang; funding acquisition: Kexin Guo, Xiang Yu, and Lei Guo; resources: Kexin Guo, Xiang Yu, and Lei Guo; supervision: Lei Guo;

Funding This work was supported in part by the National Key Research and Development Program of China (Grant Number 2022YFB4701301), the National Natural Science Foundation of China (Grant Numbers 61973012, 62388101, 62273023), the Key Research and Development Program of Zhejiang (Grant Number 2021C03158), the Major Science and Technology Innovation Program of Hangzhou (Grant Number 2022AIZD0137), and the Beijing Nova Program (Grant Number 20230484266).

Data Availability Statement Not applicable.

Declarations

Competing Interests The authors declare no conflict of interest.

References

1. Ollero, A., Tognon, M., Suarez, A., Lee, D., Franchi, A.: Past, present, and future of aerial robotic manipulators. IEEE Trans. Rob. **38**(1), 626–645 (2022). https://doi.org/10.1109/TRO.2021.3084395
2. Hamaza, S., Georgilas, I., Fernandez, M., Sanchez, P., Richardson, T., Heredia, G., Ollero, A.: Sensor installation and retrieval operations using an unmanned aerial manipulator. IEEE Robot. Autom. Lett. **4**(3), 2793–2800 (2019). https://doi.org/10.1109/LRA.2019.2918448
3. Li, L., Zhang, T., Zhong, H., Li, H., Zhang, H., Fan, S., Cao, Y.: Autonomous removing foreign objects for power transmission line by using a vision-guided unmanned aerial manipulator. J. Intell. Robot. Syst. **103**, 1–14 (2021). https://doi.org/10.1007/s10846-021-01482-3
4. Ollero, A., Heredia, G., Franchi, A., Antonelli, G., Kondak, K., Sanfeliu, A., Viguria, A., Martinez-de Dios, J.R., Pierri, F., Cortes, J., Santamaria-Navarro, A., Trujillo Soto, M.A., Balachandran, R., Andrade-Cetto, J., Rodriguez, A.: The AEROARMS project: Aerial robots with advanced manipulation capabilities for inspection and maintenance. IEEE Robot. Autom. Mag. **25**(4), 12–23 (2018). https://doi.org/10.1109/MRA.2018.2852789
5. Jimenez-Cano, A.E., Sanchez-Cuevas, P.J., Grau, P., Ollero, A., Heredia, G.: Contact-based bridge inspection multirotors: Design, modeling, and control consideringthe ceiling effect. IEEE Robot.

Autom. Lett. **4**(4), 3561–3568 (2019). https://doi.org/10.1109/LRA.2019.2928206
6. Sun, Y., Jing, Z., Dong, P., Huang, J., Chen, W., Leung, H.: A switchable unmanned aerial manipulator system for window-cleaning robot installation. IEEE Robot. Autom. Lett. **6**(2), 3483–3490 (2021). https://doi.org/10.1109/LRA.2021.3062795
7. Ruggiero, F., Lippiello, V., Ollero, A.: Aerial manipulation: A literature review. IEEE Robot. Autom. Lett. **3**(3), 1957–1964 (2018). https://doi.org/10.1109/LRA.2018.2808541
8. Pounds, P.E.I., Dollar, A.M.: Stability of helicopters in compliant contact under PD-PID control. IEEE Trans. Rob. **30**(6), 1472–1486 (2014). https://doi.org/10.1109/TRO.2014.2363371
9. Kondak, K., Huber, F., Schwarzbach, M., Laiacker, M., Sommer, D., Bejar, M., Ollero, A.: Aerial manipulation robot composed of an autonomous helicopter and a 7 degrees of freedom industrial manipulator. In: Proc. IEEE Int. Conf. Robot. Autom., pp. 2107–2112 (2014). https://doi.org/10.1109/ICRA.2014.6907148
10. McArthur, D.R., Chowdhury, A.B., Cappelleri, D.J.: Autonomous door opening with the interacting-boomcopter unmanned aerial vehicle. J. Mech. Robot **12**(2) (2020). https://doi.org/10.1115/1.4045843
11. Kremer, P., Sanchez-Lopez, J.L., Voos, H.: A hybrid modelling approach for aerial manipulators. J. Intell. Robot. Syst. **105**(4), 74 (2022). https://doi.org/10.1007/s10846-022-01640-1
12. Caballero, A., Suarez, A., Real, F., Vega, V.M., Bejar, M., Rodriguez-Castaño, A., Ollero, A.: First experimental results on motion planning for transportation in aerial long-reach manipulators with two arms. In: Proc. IEEE/RSJ Int. Conf. Intell. Robots Syst., pp. 8471–8477 (2018). https://doi.org/10.1109/IROS.2018.8594123
13. Suarez, A., Jimenez-Cano, A.E., Vega, V.M., Heredia, G., Rodriguez-Castaño, A., Ollero, A.: Design of a lightweight mechatronics system for aerial manipulation. Mechatronics **50**, 30–44 (2018). https://doi.org/10.1016/j.mechatronics.2018.01.005
14. Kamel, M., Verling, S., Elkhatib, O., Sprecher, C., Wulkop, P., Taylor, Z., Siegwart, R., Gilitschenski, I.: The voliro omniorientational hexacopter: An agile and maneuverable tiltable-rotor aerial vehicle. IEEE Robot. Autom. Mag. **25**(4), 34–44 (2018). https://doi.org/10.1109/MRA.2018.2866758
15. Bodie, K., Brunner, M., Pantic, M., Walser, S., Pfändler, P., Angst, U., Siegwart, R., Nieto, J.: Active interaction force control for contact-based inspection with a fully actuated aerial vehicle. IEEE Trans. Rob. **37**(3), 709–722 (2021). https://doi.org/10.1109/TRO.2020.3036623
16. Mellinger, D., Lindsey, Q., Shomin, M., Kumar, V.: Design, modeling, estimation and control for aerial grasping and manipulation. In: 2011 Proc. IEEE/RSJ Int. Conf. Intell. Robots Syst., pp. 2668–2673 (2011). https://doi.org/10.1109/IROS.2011.6094871
17. Tognon, M., Chávez, H.A.T., Gasparin, E., Sablé, Q., Bicego, D., Mallet, A., Lany, M., Santi, G., Revaz, B., Cortés, J., Franchi, A.: A truly-redundant aerial manipulator system with application to push-and-slide inspection in industrial plants. IEEE Robot. Autom. Lett. **4**(2), 1846–1851 (2019). https://doi.org/10.1109/LRA.2019.2895880
18. Kanellakis, C., Nikolakopoulos, G.: Guidance for autonomous aerial manipulator using stereo vision. J. Intell. Robot. Syst. **100**(3–4), 1545–1557 (2020). https://doi.org/10.1007/s10846-019-01060-8
19. Coelho, A., Sarkisov, Y., Wu, X., Mishra, H., Singh, H., Dietrich, A., Franchi, A., Kondak, K., Ott, C.: Whole-body teleoperation and shared control of redundant robots with applications to aerial manipulation. J. Intell. Robot. Syst. **102**, 1–22 (2021). https://doi.org/10.1007/s10846-021-01365-7
20. Bodie, K., Tognon, M., Siegwart, R.: Dynamic end effector tracking with an omnidirectionalparallel aerial manipulator. IEEE Robot. Autom. Lett. **6**(4), 8165–8172 (2021). https://doi.org/10.1109/LRA.2021.3101864
21. Paul, H., Miyazaki, R., Ladig, R., Shimonomura, K.: Landing of a multirotor aerial vehicle on an uneven surface using multiple on-board manipulators. In: Proc. IEEE/RSJ Int. Conf. Intell. Robots Syst., pp. 1926–1933 (2019). https://doi.org/10.1109/IROS40897.2019.8968529
22. Guo, K., Jia, J., Yu, X., Guo, L., Xie, L.: Multiple observers based anti-disturbance control for a quadrotor UAV against payload and wind disturbances. Control Eng. Pract. **102**, 104560 (2020). https://doi.org/10.1016/j.conengprac.2020.104560
23. Wang, S., Chen, J., He, X.: An adaptive composite disturbance rejection for attitude control of the agricultural quadrotor UAV. ISA Trans. **129**, 564–579 (2022). https://doi.org/10.1016/j.isatra.2022.01.012
24. Jia, J., Guo, K., Yu, X., Guo, L., Xie, L.: Agile flight control under multiple disturbances for quadrotor: Algorithms and evaluation. IEEE Trans. Aerosp. Electron. Syst. **58**(4), 3049–3062 (2022). https://doi.org/10.1109/TAES.2022.3143781
25. Kim, S., Choi, S., Kim, H., Shin, J., Shim, H., Kim, H.J.: Robust control of an equipment-added multirotor using disturbance observer. IEEE Trans. Control Syst. Technol. **26**(4), 1524–1531 (2018). https://doi.org/10.1109/TCST.2017.2711602
26. Zhang, G., He, Y., Dai, B., Gu, F., Han, J., Liu, G.: Robust control of an aerial manipulator based on a variable inertia parameters model. IEEE Trans. Ind. Electron. **67**(11), 9515–9525 (2020). https://doi.org/10.1109/TIE.2019.2956414
27. Aydemir, M., Arıkan, K.B.: Evaluation of the disturbance rejection performance of an aerial manipulator. J. Intell. Robot. Syst. **97**, 451–469 (2020). https://doi.org/10.1007/s10846-019-01013-1
28. Nava, G., Sablé, Q., Tognon, M., Pucci, D., Franchi, A.: Direct force feedback control and online multi-task optimization for aerial manipulators. IEEE Robot. Autom. Lett. **5**(2), 331–338 (2019). https://doi.org/10.1109/LRA.2019.2958473
29. Ryll, M., Muscio, G., Pierri, F., Cataldi, E., Antonelli, G., Caccavale, F., Bicego, D., Franchi, A.: 6D interaction control with aerial robots: The flying end-effector paradigm. Int. J. Robot. Res. **38**(9), 1045–1062 (2019). https://doi.org/10.1177/0278364919856694
30. Lee, D., Seo, H., Jang, I., Lee, S.J., Kim, H.J.: Aerial manipulator pushing a movable structure using a DOB-based robust controller. IEEE Robot. Autom. Lett. **6**(2), 723–730 (2021). https://doi.org/10.1109/LRA.2020.3047779
31. Cuniato, E., Lawrance, N., Tognon, M., Siegwart, R.: Power-based safety layer for aerial vehicles in physical interaction using Lyapunov exponents. IEEE Robot. Autom. Lett. **7**(3), 6774–6781 (2022). https://doi.org/10.1109/LRA.2022.3176959
32. Zhang, W., Liu, Q., Wang, M., Jia, J., Lyu, S., Guo, K., Yu, X., Guo, L.: Design of an aerial manipulator system applied to capture missions. Proc. Int. Conf. Unmanned Aircr. Syst., 1063–1069 (2021). https://doi.org/10.1109/ICUAS51884.2021.9476743
33. Falk, A.R., Martin, L.D., Hasiotis, S.T.: A morphologic criterion to distinguish bird tracks. J. Ornithol. **152**(3), 701–716 (2011). https://doi.org/10.1007/s10336-011-0645-x
34. Welde, J., Paulos, J., Kumar, V.: Dynamically feasible task space planning for underactuated aerial manipulators. IEEE Robot. Autom. Lett. **6**(2), 3232–3239 (2021). https://doi.org/10.1109/LRA.2021.3051572
35. Garofalo, G., Beck, F., Ott, C.: Task-space tracking control for underactuated aerial manipulators. In: 2018 Eur. Control Conf., pp. 628–634 (2018). https://doi.org/10.23919/ECC.2018.8550248
36. Guo, L., Chen, W.-H.: Disturbance attenuation and rejection for systems with nonlinearity via DOBC approach. Int. J. Robust Nonlinear Control **15**(3), 109–125 (2005). https://doi.org/10.1002/rnc.978

37. Yu, X., Zhu, Y., Qiao, J., Guo, L.: Anti-disturbance controllability analysis and enhanced antidisturbance controller design with application to flexible spacecraft. IEEE Trans. Aerosp. Electron. Syst. **57**(5), 3393–3404 (2021). https://doi.org/10.1109/TAES.2021.3079566
38. Zhu, Y., Guo, L., Qiao, J., Li, W.: An enhanced anti-disturbance attitude control law for flexible spacecrafts subject to multiple disturbances. Control Eng. Pract. **84**, 274–283 (2019). https://doi.org/10.1016/j.conengprac.2018.11.001

Qianyuan Liu received the B.S. degree and M.S. degree in control science and engineering from Shandong University, China, in 2016 and 2019, respectively. Since September 2019, he has been a Ph.D. student in School of automation science and electrical engineering of Beihang University. His research interests include aerial manipulator, intelligent control of robotic systems, physical human-robot interaction.

Yuhang Liu received the B.S. degree in aircraft control and information engineering from Northwestern Polytechnical University, Xi'an, China, in 2023. He is currently working toward the M.S. degree in mechanical engineering with the School of Aeronautic Science and Engineering, Beihang University, Beijing, China. His current research interests include accurate and intelligent control of robotic systems.

Zeshuai Chen received the B.S. degree in aircraft control and information engineering from Northwestern Polytechnical University, Xi'an, China, in 2022. He is currently working toward the Ph. D. degree in School of Automation Science and Electrical Engineering from Beihang University, Beijing, China. His research interests include aerial manipulator and control of robotic systems.

Kexin Guo received the B.S. degree in control theory and control engineering from Beijing Institute of Technology, Beijing, China, in 2011, the M.S. degree in instrumentation science and technology from Beihang University, Beijing, in 2014, and the Ph.D. degree in electrical and electronic engineering from Nanyang Technological University, Singapore, in 2018. He was a Post-Doctoral Fellow of the "Zhuoyue" program with the School of Automation Science and Electrical Engineering, Beihang University in 2019. Since 2021, he has been an Associate Professor with the School of Aeronautic Science and Engineering, Beihang University, Beijing. Prof. Guo was a recipient of the Best Paper and Best Paper Finalist at international conferences. His current research interests include GNSS-denied localization, bio-inspired control and safety control of unmanned aerial vehicles.

Xiang Yu received the B.S., M.S., and Ph.D. degrees in automation science and engineering from Northwestern Polytechnical University, Xi'an, China, in 2003, 2004, and 2008, respectively. He is currently a Professor with the School of Automation Science and Electrical Engineering, Beihang University, Beijing, China. He was a Post-Doctoral Research Fellow with the Department of Electrical and Computer Engineering, Western University, London, ON, Canada, and a Research Associate with the Department of Mechanical, Industrial and Aerospace Engineering, Concordia University, Montreal, QC, Canada. He has authored over 70 prestigious journal papers and a monograph, including IEEE Transactions, AIAA Journals, and Progress in Aerospace Sciences. His current research interests include safety control of unmanned aerial vehicles, autonomous navigation and control of hypersonic vehicles. Prof. Yu was a recipient of the Recruitment Program for Young Professionals, First Prize of Science and Technology Progress Award of China Instrument and Control Society, Youth Science and Technology Award of Chinese Society of Aeronautics and Astronautics, the Best Paper and Best Paper Finalist at international conferences. He has also served as the Associate Editors of Journal of Field Robotics, Journal of Intelligent & Robotic Systems, Asian Journal of Control, and Chinese Journal of Aeronautics, Program Co-Chair, Invitation Chair, and IPC Member of several academic conferences.

Youmin Zhang (Senior Member, IEEE) received the B.S., M.S., and Ph.D. degrees in automatic control from Northwestern Polytechnical University, Xi'an, China, in 1983, 1986, and 1995, respectively. He is currently a Professor with the Department of Mechanical, Industrial and Aerospace Engineering, Concordia University, Montreal, QC, Canada. He has authored four books, over 500 journal and conference papers, and book chapters. His current research interests include fault diagnosis and fault-tolerant control, cooperative guidance, navigation, and control (GNC) of unmanned aerial/space/ground/surface vehicles, with applications to remote sensing, and renewable energy and smart grids. Prof. Zhang is a Registered Professional Engineer, an Editorial Board Member, the Editor-in-Chief, the Editor-at-Large, the Editor, or the Associate Editor of several international journals (e.g., IEEE TRANSACTIONS ON NEURAL NETWORKS AND LEARNING SYSTEMS). He has served as the General Chair, the Program Chair, and the IPC Member of several unmanned systems and energy-relevant international conferences. He is the President of International Society of Intelligent Unmanned Systems and a member of the Technical Committee for several scientific societies. He is a Fellow of CSME and a Senior Member of AIAA.

Lei Guo was born in Qufu, China, in 1966. He received the B.S. degree and the M.S. degree from Qufu Normal University, in 1988 and 1991, respectively, and the Ph.D. degree from Southeast University, Nanjing, China, in 1997. From 1991 to 1994, he was a Lecturer with Qingdao University, Qingdao, China. From 1997 to 1999, he was a Postdoctoral Fellow and Associate Fellow with Southeast University. From 1999 to 2000, he was a Postdoctoral Fellow with IRCCyN, Nantes, Frances. From 2000 to 2005, he was a Research Associate/Fellow/Visiting Professor with Loughborough University, UMIST and Manchester University, U.K. From 2004 to 2006, he was a professor with Southeast University, now he is a Guest Chair Professor. From 2006 to now, he is a Distinguish Professor and Director of the Space Intelligent Control Research Center at Beihang University, Beijing, China. He is an Academician of the Chinese Academy of Sciences (CAS), a Fellow of IEEE, IET, Chinese Association of Automation (CAA), and China Association of Inventions (CAI). He is the Director of the Navigation, Guidance and Control Committee of the CAA. His research interests include anti-disturbance control theory and applications, intelligent navigation and control technology of unmanned systems. He has published more than 480 papers, 7 monographs, and has more than 180 authorized invention patents. He was the recipient of the National Nature Science Awards (2013), National Technology Invention Awards (2018), National Pioneer Innovation Award (2023) of China. He also obtained the Gold Medal of International Exhibition of Inventions of Geneva, Nuremberg and Turkey for bio-inspired navigation sensor, compound-eye-inspired navigation systems and biomimetic flying robots, respectively.

Authors and Affiliations

Qianyuan Liu[1] · Yuhang Liu[2] · Zeshuai Chen[1] · Kexin Guo[2,3] · Xiang Yu[1,3] · Youmin Zhang[4] · Lei Guo[1,3]

Qianyuan Liu
liuqianyuan@buaa.edu.cn

Yuhang Liu
lyhbuaa@buaa.edu.cn

Zeshuai Chen
zschen@buaa.edu.cn

Youmin Zhang
ymzhang@encs.concordia.ca

Lei Guo
lguo@buaa.edu.cn

1 School of Automation Science and Electrical Engineering, Beihang University, 37 Xueyuan Road, Beijing 100191, China

2 School of Aeronautic Science and Engineering, Beihang University, 37 Xueyuan Road, Beijing 100191, China

3 Hangzhou Innovation Institute, Beihang University, Changhe Street, Hangzhou 310051, China

4 Department of Mechanical, Industrial and Aerospace Engineering, Concordia University, Montreal H3G 1M8, QC, Canada